2010-01-01

Internal Wave Signature Analyses with Synthetic Aperture Radar Images in the Mid-Atlantic Bight

Jingshuang Xue
University of Miami, jxue@rsmas.miami.edu

UNIVERSITY OF MIAMI

INTERNAL WAVE SIGNATURE ANALYSES WITH SYNTHETIC APERTURE RADAR IMAGES IN THE MID-ATLANTIC BIGHT

By

Jingshuang Xue

A THESIS

Submitted to the Faculty
of the University of Miami
in partial fulfillment of the requirements for
the degree of Master of Science

Coral Gables, Florida

June 2010

UNIVERSITY OF MIAMI

A thesis submitted in partial fulfillment of
the requirements for the degree of
Master of Science

INTERNAL WAVE SIGNATURE ANALYSES WITH SYNTHETIC APERTURE RADAR IMAGES IN THE MID-ATLANTIC BIGHT

Jingshuang Xue

Approved:

_____ Hans C. Graber, Ph.D. Professor of Applied Marine Physics	_____ Terri A. Scandura, Ph.D. Dean of the Graduate School
_____ Michael G. Brown, Ph.D. Professor of Applied Marine Physics	_____ Roland Romeiser, Ph.D. Professor of Applied Marine Physics

_____
Karl R. Helfrich, Ph.D.
Professor of Marine Physics
Senior Scientist of Physical Oceanography
Woods Hole Oceanographic Institution
Woods Hole, Massachusetts

XUE, JINGSHUANG (M.S., Applied Marine Physics)

Internal Wave Signature Analyses with Synthetic Aperture Radar Images in the Mid-Atlantic Bight (June 2010)

Abstract of a thesis at the University of Miami.

Thesis supervised by Professor Hans C. Graber.
No. of pages in text. (73)

57 synthetic aperture radar (SAR) images were collected over the Mid-Atlantic Bight (MAB) during the Shallow Water 2006 experiment (SW06). The dependence of internal wave (IW) signature occurrences and types in SAR images on the wind conditions is studied. A defined signature mode parameter (S_m) quantifies the signature of the IW intensity profile in relation to the mean backscatter in the image background to determine different IW types (single positive, single negative and double sign). The statistical results show that moderate wind speeds of 4-7 m/s are favorable for imaging IWs by SAR, whereas very few IW signatures are observed when the wind speed is higher than 10 m/s and lower than 2 m/s. Many S_m values are larger than 1 (positive signature) even when the angles between the wind direction and IW propagation direction ($\theta_{Wind-IW}$) are less than 90^o in the MAB, which does not agree with the result of da Silva et al. (2002). An advanced radar imaging model has been run for different wind conditions, radar look directions and IW amplitudes. The model results indicate that the proportion of S_m values larger than 1, when $\theta_{Wind-IW} < 90^o$, increases with IW amplitudes. In general, relating IW signature types mainly to the wind direction is an oversimplification without considering other factors such as look directions and IW amplitudes. An IW interaction

pattern has been studied on the basis of two sequential images from ERS2 and ENVISAT with a time lag of 28 minutes and temperature and current measurements from moorings. Phase velocities of the pattern can be derived by two-dimensional cross correlation of two images or in-situ measurements. In this pattern, the IW packet with a larger amplitude shifts less while the one with a smaller amplitude shifts more due to the interaction. The strong intensity in the interaction zone implies an amplitude increase. The intensity changes in the same IW packet after the interaction implies the energy exchange. All the characteristics agree well with the dynamics of the two-soliton pattern with a negative phase shift, according to Peterson and van Groesen (2000).

TABLE OF CONTENTS

Page

LIST OF FIGURES

LISF OF TABLES

CHAPTER 1 INTRODUCTION

This chapter first provides background information on internal wave (IW) analysis using synthetic aperture radar (SAR) and in-situ measurements. IW in this study refers low mode horizontally propagating IW in particular. Second, the motivation and objectives of the study are presented. Lastly, the organization of the thesis is provided.

1.1 Background

Tidally induced IWs are generated in a stratified ocean, by the interaction of a tidal flow with irregular topography such as sills, canyons, and continental shelf breaks (Holloway et al., 1997), which are ubiquitous features within the ocean (Figure 1.1).

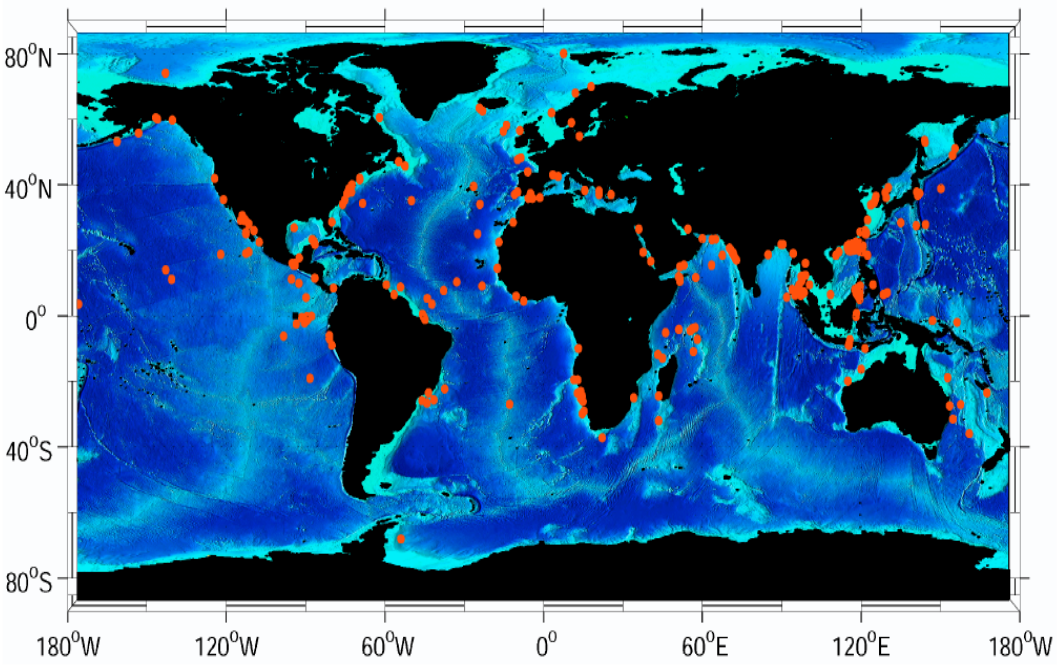

Figure 1.1 Locations of observed soliton occurrences around the world. Most locations were detected in satellite imagery. As additional data and imagery are collected, the number of noted occurrence locations will certainly increase (Apel, 2004).

IWs occur as groups or packets of oscillations with the numbers of cycles varying from a very few to a few dozen, depending on age and distance from the generation point. Although there are different generating mechanisms of IWs, they are generally considered to be tidally induced. Figure 1.2 shows a schematic of IW features in both horizontal plan and profile views. In this Figure, the rightmost wave crest is just generated by offshore tide flow at the shelf break, whereas the leftmost one is the result of a previous semidiurnal tide. C_r, 2η and λ_0 are the wave crest length, amplitude and wavelength, respectively. $c_o T$ is the distance between packet centroids, and $V_{\max} T$ is the internal tidal wavelength.

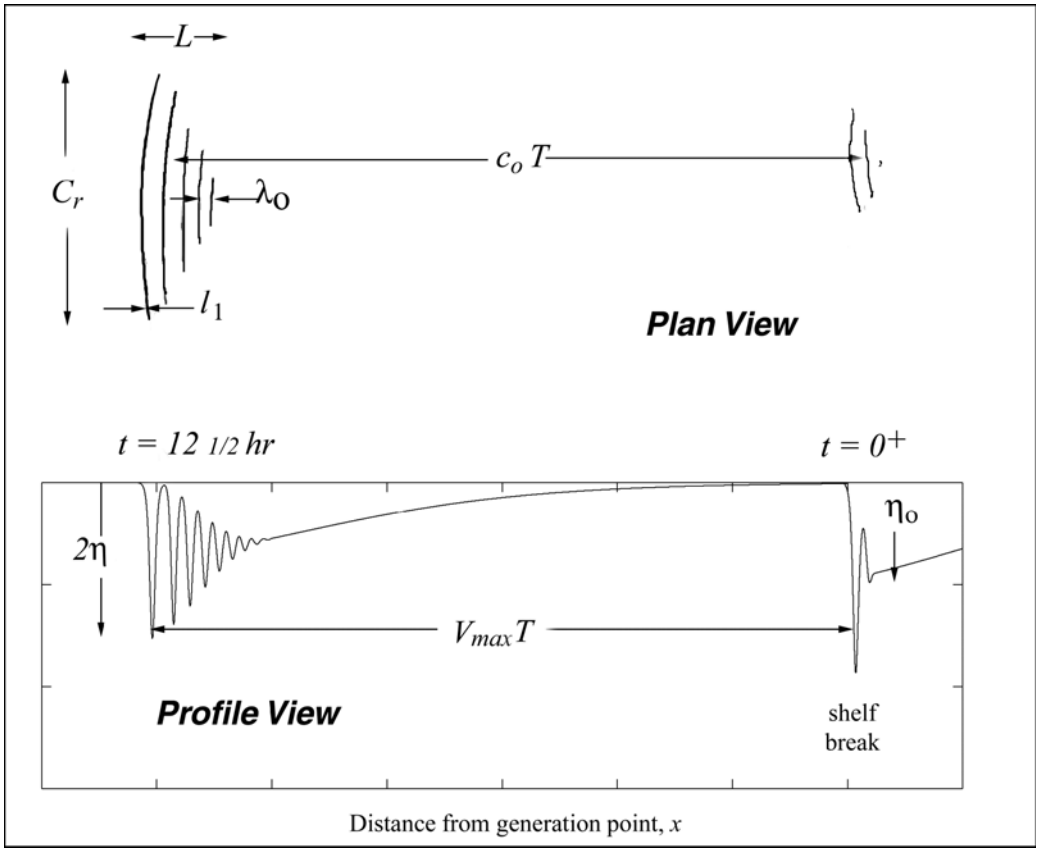

Figure 1.2 Schematic showing tidally-generated solitons on the continental shelf. $V_{\max} T$ is the internal tidal wavelength; $c_o T$ is the distance between packet centroids (Apel, 2004).

IWs are very important for many practical reasons. They can propagate over several hundred kilometers and transport both mass and momentum. These waves significantly disturb the current, density and temperature fields during passage. The temperature perturbation can cause large fluctuations in the sound speed and thus affect acoustic signal propagation in the water (Apel et al., 1997). Moreover, the considerable shear IWs carry can lead to turbulence and mixing, which can initiate the bottom sediment re-suspension (Bogucki et al., 1997; Chen and Hsu, 2005; Chen, 2007; Chen et al., 2007) and mix the nutrients into the photic zone (Holligan et al., 1985), thereby fertilizing the local region and impacting the local biology system. In fact, an early motivation for studying IWs was the unexpectedly large stress they imposed on offshore oil-drilling rigs. The role of IWs in vertical mixing of the world's ocean is also believed to be an important factor in maintaining the ocean structure and circulation (Killworth, 1998), and also in determining heat transfer between the ocean and atmosphere.

SAR, with its all weather, all day ability, high spatial resolution and wide coverage, provides an efficient method to study general IW properties and IW spatial distribution. IW distribution observed from SAR can be used as a reference when setting up a field experiment to study IW characteristics in a large area (Zheng *et al*., 2007). Past and present SAR sensors have been operated by the United States, Canada, Europe, Russia and Japan. The most recent and well-known SARs include those aboard European Remote-sensing Satellites (ERS1&2), Environmental Satellite (ENVISAT), and Canada's earth observation satellite (RADARSAT).

There are two radar imaging mechanisms for observing IWs in SAR images based on the effects of surface films and hydrodynamic wave-current interaction. The first mechanism is often active in coastal waters, where surface films, either of natural or anthropogenic origin, are present. These films accumulate in flow convergence zones, strongly damping the short surface waves and resulting in dark streaks (reduced radar backscatter) on a uniform bright background (Alpers, 1985). The surface film mechanism has two limitations. First, it is not applicable under high wind conditions. When the surface wind is high, surface films cannot accumulate on the ocean surface and affect the surface roughness in the IW field. Second, even in moderate wind conditions, most of the radar signatures have bright and dark streaks in the images, which cannot be explained by this mechanism. The hydrodynamic interaction mechanism is more adequate to explain this kind of IW signature. The whole imaging process mainly includes three parts: 1) the IW-induced current field variation, 2) the current interaction with the short wind-driven surface waves, and 3) the radar backscattering mechanism (Alpers, 1985). In other words, local currents induced by IWs can modulate sea surface capillary and short gravity waves into smooth divergent and rough convergent zones. SAR image intensities are sensitive to the sea surface roughness through the Bragg scattering mechanism. As a result, IW signatures are denoted by alternating brighter and the darker stripes corresponding to the rougher and smoother areas on the sea surface (Figure 1.3). Figure 1.4 illustrates a typical IW signature in a SAR image.

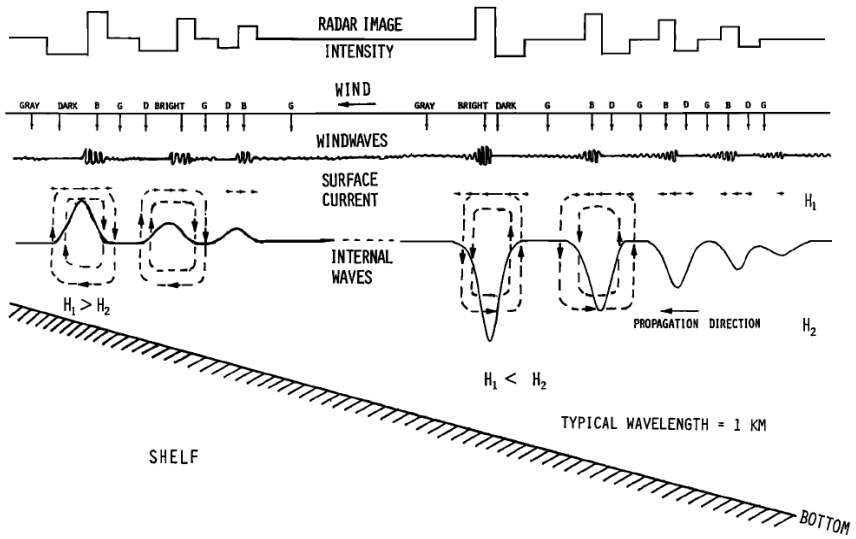

Figure 1.3 Schematic diagram of interaction of IWs, surface current field, wind waves, and resultant SAR image intensity variation (Liu et al., 1998).

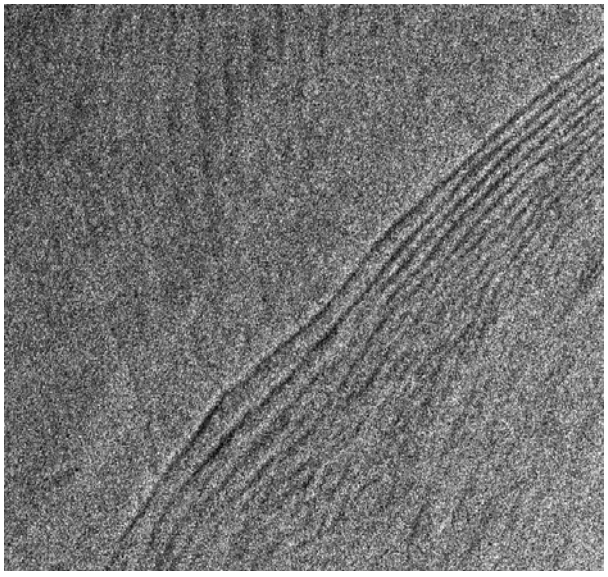

Figure 1.4 Example of an IW signature in a SAR image.

There are many factors affecting IW signatures in SAR images such as radar parameters and IW-related parameters. Yang et al. (2000) examined the relationship between IW signature modulation depth and these factors using a simulation model based on the simple bragg imaging model of IWs. Results are shown in Figure 1.5. $\Delta\sigma^0$ denotes the deviation from its mean normalized radar cross section (NRCS) value. They indicate that a thinner pyconline depth, larger density variation of the pycnocline, smaller radar frequency and smaller incidence angle result in the largest modulation depth and strongest IW signatures in SAR images. In addition, 0° and 180° are optimal directions for the angle between the radar look direction and IW propagation direction ($\theta_{Look-IW}$), for SAR observation.

Actually, IW signatures in SAR images depend not only on the dynamic characteristics of the interior ocean and radar parameters, but also on phenomena taking place at the air-sea interface such as surface roughness variability and wave damping due to the presence of surface films (da Silva et al., 1998).

Da Silva et al. (1998) first summarized three different types of IW signatures in SAR in the continental shelf region of the western Iberian, which can not be explained by Yang et al., 2000's simulation results. These signatures include: 1) positive and negative backscatter variations from the mean background level (designated by brighter-darker double-signed signatures), 2) predominant negative variations relative to the mean (single-negative), and 3) predominant positive variations departing from the background (single-positive). These three different types can be quantified by a signature mode parameter (S_m) defined as the quotient between the strengths of the positive and negative parts of the signatures.

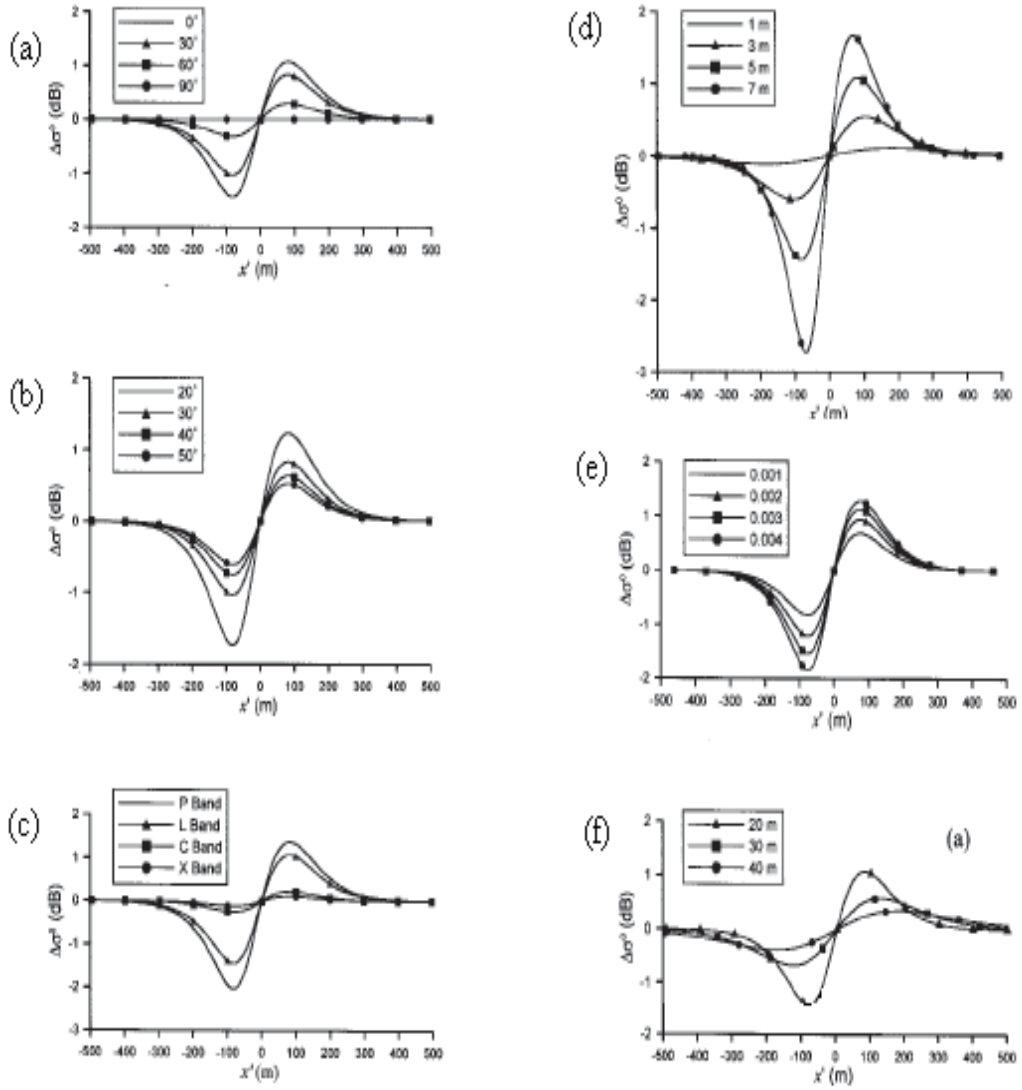

Figure 1.5 (a) $\Delta\sigma^0$ under different radar look directions (b) $\Delta\sigma^0$ under different radar incidence angles (c) $\Delta\sigma^0$ under different radar bands (d) $\Delta\sigma^0$ under different IW amplitudes (e) $\Delta\sigma^0$ under different density variations of pycnocline (f) $\Delta\sigma^0$ under different pyconcline depths for depression wave (Yang et al., 2000).

In the paper by da Silva et al. (1998), the last case was identified primarily when the background backscatter level was near to the radar "noise floor" which is the minimum radar intensity above which variations can be measured. Later da Silva et al. (1999) reported long IWs with wavelengths of up to several kilometers and high phase velocities (C>1 m/s) displaying positive backscatter variations relative to a background above the noise level.

These different types of signatures were interpreted assuming that advection of surfactant films play an essential role in the modulation of the surface-wave spectrum by the IW surface currents. Although this result agrees with observation, the study by Brandt et al. (1999) suggested that IW signatures have dependence on the wind direction relative to the IW propagation direction ($\theta_{Wind-IW}$) and the wind speed by using numerical simulations of normalized radar cross section variations with an advanced radar imaging model (composite surface model). Inclusion of the effects of wind conditions on the different IW signatures shows that the wind can also produce three IW signature types. This complements the surface film theory of da Silva et al. (1998) because the role of surface films is negligible when the surface wind is high. Da Silva et al. (2002) examined the role of wind direction on SAR signature types in the western Iberian shelf (the west of Portugal) and suggested that IWs propagating against the wind direction were imaged primarily as positive signatures, while those propagating in the wind direction were mostly negative sign signatures by using a wind contrast model based on a simple first-order Bragg scattering theory and hydrodynamic modulation theory. A comprehensive understanding of all these IW signature types and their causes is important for an accurate

interpretation of SAR IW signatures, especially in those cases where no in-situ measurements are available.

Besides the clear understanding of different IW signature types in SAR imagery, accurate interpretation of IW properties such as wavelength, phase velocity, amplitude, and interior ocean parameters such as pycnocline depth is also an important issue. In fact, much effort has been put into the IW parameters estimation from SAR signatures in the recent years. IW wavelength is very straightforward to estimate, defined as the distance between successive peaks along a radar intensity profile. For IW phase velocities, the traditional method is to measure the distance between successive IW groups divided by a tidal period. In order to understand more details about IW properties and ocean environment parameters from SAR images, a solitary wave theory that describes the evolution of nonlinear IWs has been developed. It includes effects of vertical shear, variable bottom topography, radial spreading, shoaling, and dissipation (Liu, 1985). Porter and Thompson (1999) estimated the thickness and density of the surface layer from the dispersion relation obtained from a two-layer model. Li et al. (2000) estimated the mixed layer depth in the Mid-Atlantic Bight (MAB) by matching theoretical wave speed of a two-layer model with wave speeds measured from SAR images, assuming a semidiurnal tide origin for these IWs. Zheng et al. (2001) determined the soliton characteristic half width based on a theoretical expression for an ocean internal soliton in SAR. Yang et al. (2003) estimated IW amplitudes in the South China Sea by matching with wave speed and characteristic half-width measured from SAR signatures. Zhao et al. (2004) estimated ocean stratification structure in a two-layer model based on the polarity conversion of IW. Although we could get some reasonable estimation of IW properties in

some case studies using the methods above, we still need to put more effort into this study due to its limited generality.

Although SAR is very efficient in detecting IWs, it has a large limitation in studying short time scale IW features such as IW interaction and IW refraction due to its long temporal sampling interval. This can be solved by using sequential images from different sensors or sensors of the same type on from different satellites within a short time interval, such as ERS-2 and ENVISAT or ERS-2 and Moderate Resolution Imaging Spectroradiometer (MODIS) (Mitnik, 2007, Zhao et al. 2008). With the fusion of these images, phase speeds can be derived for all IW packets by determining the spatial shift between sequential images, which makes the study of IW interaction and refraction possible. It has a big advantage over the single-image-based method, where it is often hard to determine two sequential IW packets when the IW pattern is very complex or there are no two sequential IW packets in the SAR image.

It is true that we can get a lot of IW information from satellite images as mentioned above. However, in order to obtain a full characterization of the observed event in SAR images, it needs to be complemented with data from in-situ sampling devices. For example, temperature sensors and acoustic Doppler current profilers (ADCP) can record the disturbances within the water column during IW passing. With a mooring array along the propagation direction of IWs, the IW evolution can be studied. Large IW initiated field experiments have been carried out in different areas such as the 1995 Shallow Water Acoustics in a Random Medium experiment in the MAB and the 1999/2001 Asia Seas International Acoustics Experiment in the South China Sea. In such field experiments, Conductivity-Temperature-Depth (CTD) casts near the specific IW area can give a timely

measurement of environmental parameters such as density and buoyancy frequency with depth. Echo-sounders and other profilers will give more information. For a specific case study, we can get the amplitude, phase velocity and wavelength estimation from the field measurement and make a comparison with the result obtained from SAR images.

1.2 Motivation

IW signatures in SAR imagery are affected by many factors, such as radar parameters, IW parameters, dynamic characteristics of the interior ocean, wind conditions, surface film etc. IW signatures can be characterized by three different types. Clearly understanding the types and correctly interpreting IW signatures is very important, especially in the areas where in-situ measurements are not available.

In the Shallow Water 2006 (SW06) experiment in the MAB, numerous SAR images were collected from July to September in 2006, which provided enough data to do statistics on IW signature types in this area. At the same time, the numerous in-situ measurements were available, such as wind condition, temperature profile, current profile, and CTD.

The main motivation is to exploit this nice dataset and to make full use of satellite imagery and in-situ measurement. It makes it possible to figure out the causes to the different signature types in the MAB such as IW amplitude, the wind condition etc. The other motivation is to study the IW interactions. Studies on the IW interactions on the basis of SAR imagery appear rare in the literature, which is mainly because clear IW interaction patterns are very hard to be observed in SAR images and no suitable in-situ measurements are available to measure accurate IW amplitude and phase speed in most

cases. There are many interaction patterns shown in the SAR images we collected and numerous in-situ measurements are available, which makes an IW interaction analysis possible.

1.3 Objectives

The primary objectives of this study are:

(1) To examine the relationship between the wind speed and IW occurrence in SAR images.

(2) To assess the role of wind condition on IW signature types in the MAB and to explain the statistics result by using a radar backscattering model.

(3) To study suitable IW interaction cases and make a comparison of the IW parameters before-interaction and after-interaction such as the phase speed and the amplitude by making full use of in-situ measurements and SAR images.

1.4 Organization

All datasets used in this study are described in chapter 2. Chapter 3 introduces the methods used for the data analysis. In chapter 4, three main results are presented. First, satellite-based wind data from July to September is used to examine the dependence of IW occurrence on wind speed. Second, the relative intensity of every IW packet signature in SAR images is plotted and "signature mode" value is calculated for the leading IW. The statistics of the relationship of "signature mode" value and the angle between radar

look direction and IW propagation direction is examined. Third, an IW interaction case is studied using a combination of SAR imagery and in-situ measurements.

In chapter 5, a radar imaging model is used to explain the statistical results. Model simulations are run for different angles between radar look direction and IW propagation direction and different angles between wind direction and IW propagation direction, wind speeds and IW amplitudes. A numerical two-soliton interaction simulation from the literature is used as basis for comparison with the IW interaction pattern from SAR. Chapter 6 summarizes all important findings and conclusions.

CHAPTER 2 DATASETS

From July to September 2006, the SW06 experiment, a large, multi-institution, multi-investigator project, was carried out on the continental shelf offshore New Jersey.

The MAB is characterized by a broad shelf and steep slope interrupted by numerous small canyons. The area has a significant continental shelf extending up to 250 km from shore and is influenced by the Gulf Stream circulation as well as short duration wind driven upwelling and estuarine exchanges. High-frequency nonlinear IWs are generated near the shelf break during stratified conditions (late spring to early fall) and tend to propagate toward the shelf (Apel et al., 1995). The semidiurnal tidal flow is dominated by the principal lunar constituent M2 (12.4 hour period), which propagates toward the shelf from the North Atlantic.

This experimental campaign was designed to understand the impact of nonlinear IWs on acoustic propagation and scattering in shallow water and was designed to combine a great variety of instruments on different platforms including acoustics and oceanographic moorings, aircraft, shore-based high frequency radar, Air-Sea Interaction Spar (ASIS) buoys, satellite-based SAR, and sampling devices on board research vessels.

Figure 2.1 shows the bathymetry of the study area. Contour lines indicate depths of 50 m, 100 m, 200 m, 300 m, 400 m, 500 m and 1000 m. Blue dots show the locations of ASIS buoys, and red dots are the nominal locations of the environmental moorings. The Figure gives a general idea about the moorings' setup. A more complete description of the entire experimental setting can be found in the paper by Newhall et al. (2007).

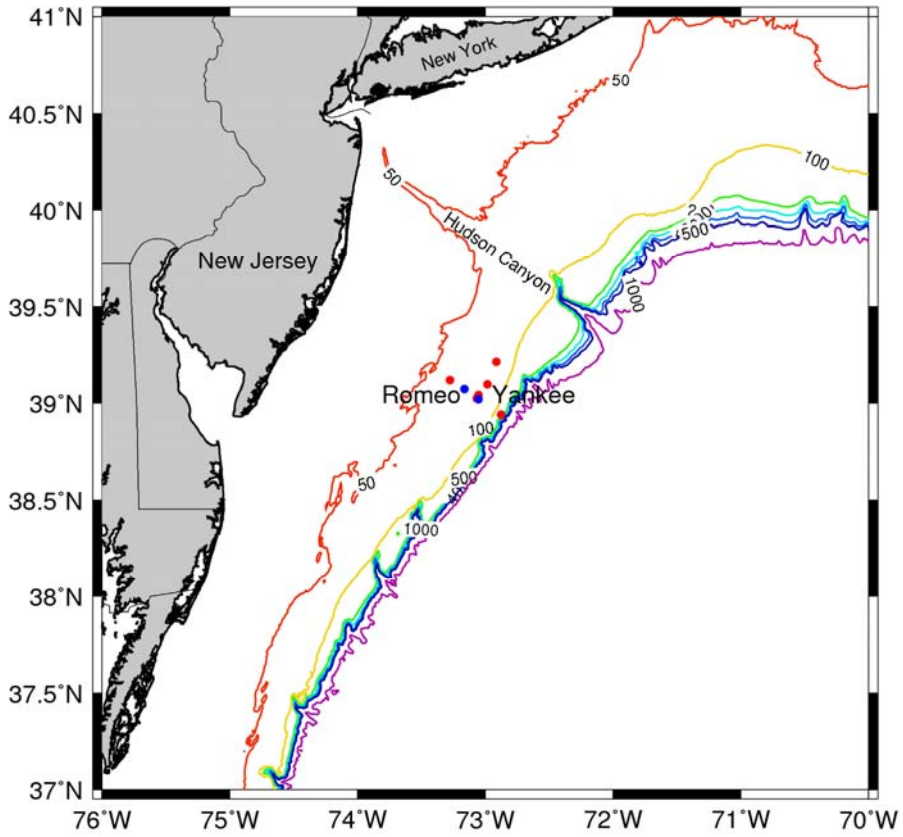

Figure 2.1 Bathymetry of the MAB. Contour lines indicate 50 m, 100 m, 200 m, 300 m, 400 m, 500 m and 1000 m. The circles show the nominal locations of the environmental moorings (red) and ASIS buoys (blue) (Caruso and Graber, 2006).

2.1 SAR Images

Between July 14 and September 26, 2006, 57 SAR images were acquired over the MAB region. There are 11 ERS2, 12 ENVISAT ASAR and 34 RADARSAT images, all of which were acquired through the University of Miami's Center for Southeastern Tropical Advanced Remote Sensing. Table 2.1 shows a list of the SAR scenes. Different beams stand for different incidence angles. ENVISAT IS2 beam mode has a center incidence angle of 23°, which is as the same as the one of ERS2. RADARSAT uses the

Standard Beam mode, which allows imaging over a wide range of incidence angles acquired in seven different modes referred to as S1 to S7. The incidence angles range from 20° at the inner edge of S1 to 49° at the outer edge of S7. VV means the signal is transmitted and received in vertical polarization whereas HH represents transmission and reception in horizontal polarization. Figure 2.2 shows the satellite imagery coverage in the experiment. Red rectangles illustrate the ENVISAT coverage; green ones denote the ERS2 coverage; and blue ones show the RADARSAT coverage. Red dots denote the environmental moorings locations and blue dots show ASIS locations

Date	Time	Satellite	Beam	Polarization
14-Jul-06	2:37	ENVISAT	IS2	VV
14-Jul-06	3:06	ERS2		VV
19-Jul-06	22:33	RADARSAT	S1	HH
23-Jul-06	15:07	ENVISAT	IS2	VV
23-Jul-06	15:36	ERS2		VV
25-Jul-06	22:58	RADARSAT	S7	HH
29-Jul-06	22:41	RADARSAT	S3	HH
30-Jul-06	2:35	ENVISAT	IS2	VV
30-Jul-06	3:03	ERS2		VV
30-Jul-06	10:55	RADARSAT	S3	HH
1-Aug-06	22:42	RADARSAT	S7	HH
2-Aug-06	2:28	ENVISAT	IS2	VV
2-Aug-06	2:57	ERS2		VV
5-Aug-06	22:37	RADARSAT	S1	HH
6-Aug-06	10:51	RADARSAT	S5	HH
8-Aug-06	15:00	ENVISAT	IS2	VV
8-Aug-06	15:28	ERS2		VV
8-Aug-06	22:38	RADARSAT	S6	HH
9-Aug-06	11:03	RADARSAT	S1	
12-Aug-06	22:33	RADARSAT	S1	HH
13-Aug-06	10:47	RADARSAT	S6	HH
15-Aug-06	22:45	RADARSAT	S4	HH
16-Aug-06	10:59	RADARSAT	S2	HH
18-Aug-06	2:37	ENVISAT	IS2	VV
18-Aug-06	3:06	ERS2		VV
18-Aug-06	22:58	RADARSAT	S7	HH
20-Aug-06	10:43	RADARSAT	S7	HH
22-Aug-06	22:41	RADARSAT	S3	HH

23-Aug-06	10:55	RADARSAT	S3	HH
25-Aug-06	22:54	RADARSAT	S7	HH
27-Aug-06	15:07	ENVISAT	IS2	VV
27-Aug-06	15:36	ERS2		VV
29-Aug-06	22:37	RADARSAT	S1	HH
30-Aug-06	10:51	RADARSAT	S5	HH
1-Sep-06	22:50	RADARSAT	S6	HH
2-Sep-06	11:04	RADARSAT	S1	HH
3-Sep-06	2:34	ENVISAT	IS2	VV
3-Sep-06	3:03	ERS2	ERS2	VV
5-Sep-06	22:33	RADARSAT	S1	HH
6-Sep-06	2:40	ENVISAT	IS2	VV
6-Sep-06	3:09	ERS2	ERS2	VV
6-Sep-06	10:47	RADARSAT	S6	HH
9-Sep-06	10:59	RADARSAT	S2	HH
11-Sep-06	22:58	RADARSAT	S7	HH
12-Sep-06	15:04	ENVISAT	IS2	VV
12-Sep-06	15:33	ERS2	ERS2	VV
13-Sep-06	10:43	RADARSAT	S7	HH
15-Sep-06	22:41	RADARSAT	S3	HH
16-Sep-06	10:55	RADARSAT	S3	HH
18-Sep-06	22:54	RADARSAT	S7	HH
22-Sep-06	2:37	ENVISAT	IS2	VV
22-Sep-06	2:54	ERS2	ERS2	VV
22-Sep-06	22:37	RADARSAT	S1	HH
23-Sep-06	10:51	RADARSAT	S5	HH
25-Sep-06	2:43	ENVISAT	IS3	HH
25-Sep-06	22:49	RADARSAT	S6	HH
26-Sep-06	11:03	RADARSAT	S1	HH

Table 2.1 List of SAR scenes acquired during SW06 experiment.

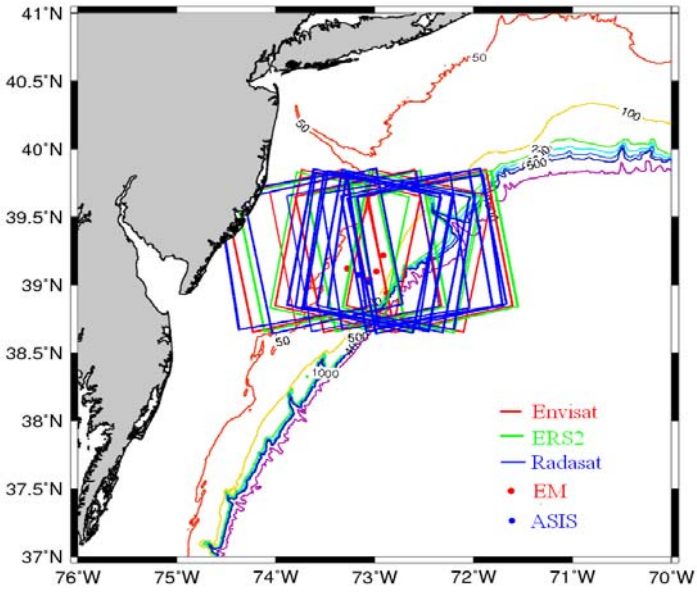

Figure 2.2 SAR coverage during the SW06 experiment. Red rectangles show the ENVISAT coverage; green ones show the ERS2 coverage; and blue ones show the RADARSAT coverage; Red dots show the environmental moorings locations; Blue dots show ASIS locations.

2.2 Moorings

A component of this experiment was a moored array of physical oceanographic sensors that was designed to measure the vertical and horizontal structure of IW fields generated at the shelf break as they propagated through the acoustics array (Irish et al., 2004). The across shelf and along shelf component of the moorings makes up a big "T" pattern in the experiment area (Figure 2.3).

Unfortunately, most of the in-situ measurements, ship-based and by the mooring array, were in the southwest part of the experiment area while most IW occurrences in the SAR images were in the northeastern. As a result, there are only a few cases that the same IW group shows up in both the SAR and in-situ data. The heavily instrumented environmental moorings SW32 and SW33 and structure mooring SW19 were used to

study an IW interaction case. ASIS buoys SW57 and SW58 were used to measure the prevailing wind conditions in the SAR imaging area.

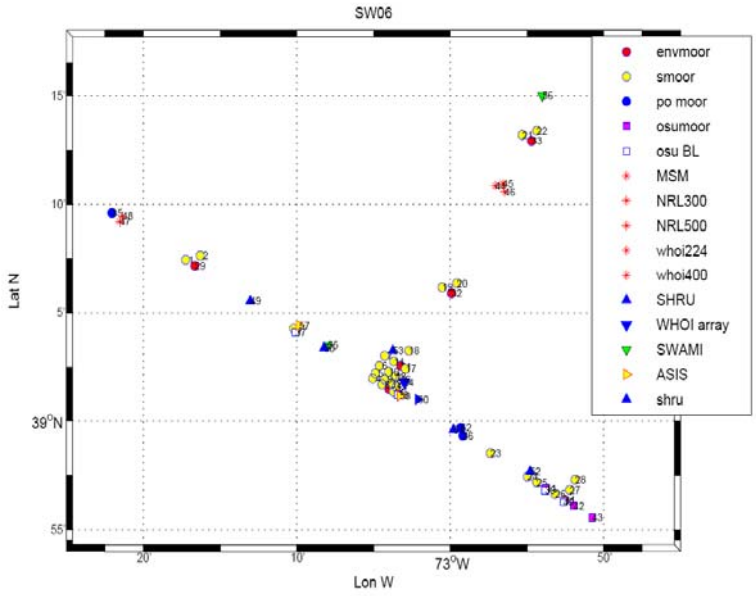

Figure 2.3 All moorings in the SW06 experiment (Newhall et al., 2007).

2.2.1 Environmental Moorings

Three of the six environmental moorings (red dots in Figure 2.3) were aligned in the across shelf direction and the other three in the along shelf direction. Environmental moorings were all subsurface with a buoyancy about 12 meters deep so the uppermost temperature, conductivity, pressure sensor was at about 14 m depth. The bottom package of ADCP and a temperature, conductivity, pressure sensor was located just above the acoustic release about 7 meters above the bottom (Irish et al., 2004). SW32 and SW33 on the along shelf leg were used in this study.

The environmental moorings were heavily instrumented. For example, SW32, located at 39.0984° N, 72.9987° W in 81 m water depth, included seven conductivity-temperature-pressure recorders distributed along the water column and a temperature

recorders located 1 m below the surface. Table 2.2 gives details of instruments on SW32 and Figure 2.4 gives a sketch of the SW32 mooring. The vertical resolution of temperature sensors was around 10 m, which is too coarse to get the accurate IW amplitude considering the relatively small IW amplitude in the MAB. However, it gives an approximate estimate of the IW amplitude. SW32 also hosted a 300 kHz upward looking ADCP at the bottom measuring water column speed profiles, particularly the vertical component which is very sensitive to IW passages. Its ensemble sampling interval was 30 seconds, which was enough to resolve the high frequency temporal variability of IW field. The vertical resolution of the ADCP was 4 m.

Overall, with these environmental moorings, we can get the temperature profile and the vertical current profile and some information about horizontal structure when IWs are passing. IW properties such as wavelength and amplitude can be estimated from these profiles directly. We can also estimate the local phase speed of IWs passing the moorings, based on the distance and time separation between the mooring and IW locations in SAR.

Instrument type	Number	Depth (m)
Mini-T	2069	1
SBE37	1770	12
SBE39	11	21
SBE37	1137	31
SBE39	12	42
SBE37	1138	53
SBE39	13	64
SBE37	1771	75
ADCP	6999	75

Table 2.2 Details of instruments on environmental mooring SW32 (Newhall et al., 2007).

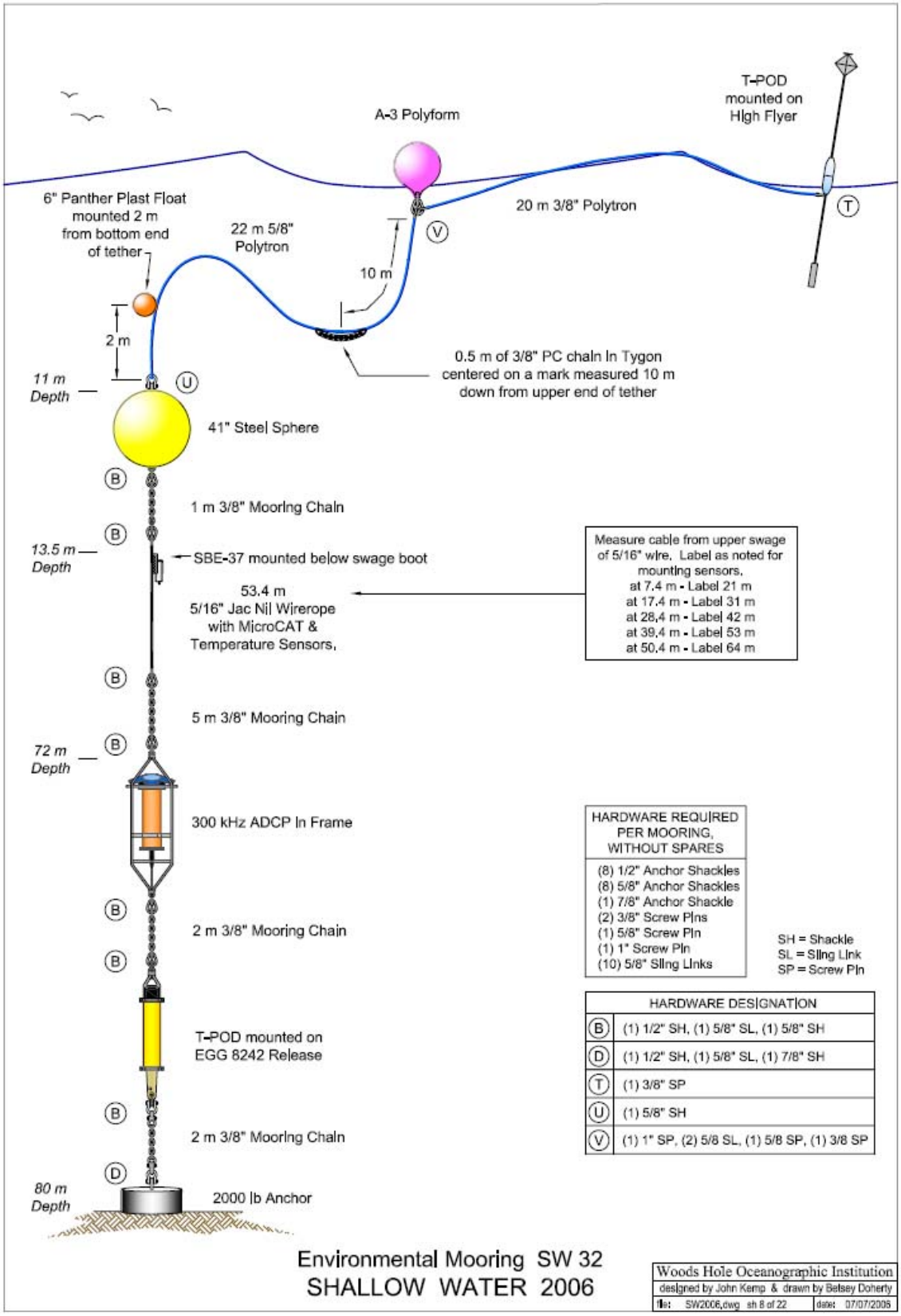

Figure 2.4 Sketch of environmental mooring SW32 (Newhall et al., 2007).

2.2.2 Structure Moorings

Two structure moorings (yellow dots in Figure 2.3) were around each of these environmental moorings. These moorings were lightly instrumented only with one CTPR and two TRs. The basic sample interval was also 30 seconds. SW19 was used in the study to make up with the missing temperature data in the SW32. Table 2.3 gives details of instruments on structure mooring SW19, and Figure 2.5 shows a sketch of the mooring's structure.

Instrument type	Number	Depth(m)
SBE39	3120	14
Mini-T	2003	25
Mini-T	2004	40

Table 2.3 Details of instruments on structure mooring SW19 (Newhall et al., 2007).

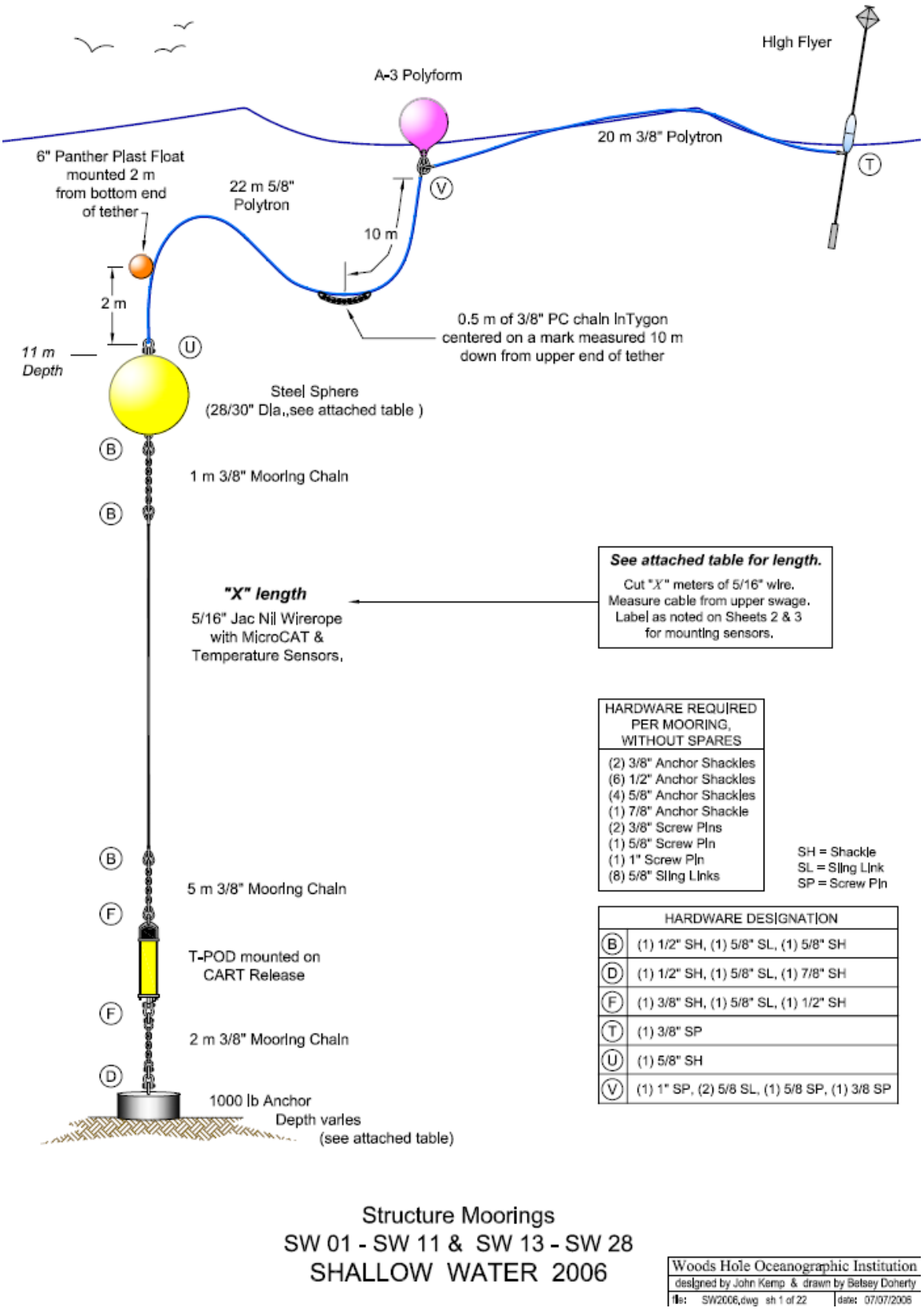

Figure 2.5 Sketch of structure mooring SW19 (Newhall et al., 2007).

2.2.3 ASIS Buoys

Two ASIS platforms (yellow triangles in Figure 2.3) were deployed within 11 km of each other at the center of the mooring array to provide local air-sea interaction observations. ASIS #1, SW57 or Yankee, was located at 39.0192° N, 73.0536° W, and ASIS #2, SW58 or Romeo, was located at 39.0739° N, 73.1641° W. Both of them worked from July 29 to September 15, 2006.

Each ASIS buoy was attached to an anchored surface buoy by floating tether. Each ASIS buoy hosted a pair of Acoustic Doppler Velocimeters at 2.5 m and 4.0 m water depth as well as depth recorders and depth-temperature recorders to characterize the temperature profile up to 7 m water depth. Additionally, the anchor line of the mooring hosted a current meter at 6 m water depth, and TR and DTR spanning from 9 to 15 m water depth. Figure 2.6 gives details of instruments on ASIS with a tether buoy.

All elevation, wind and current data are corrected for platform motions using a procedure similar to that described by Anctil et al (1994). In addition to the standard processing, the anemometer data from SW57 were corrected for a fixed rotation of 42° counterclockwise, which occurred when the instrument glanced off the R/V Knorr during deployment. Winds were then corrected to 10 m neutral values using Monin-Obukhov similarity theory as described recently in Drennan and Shay (2006).

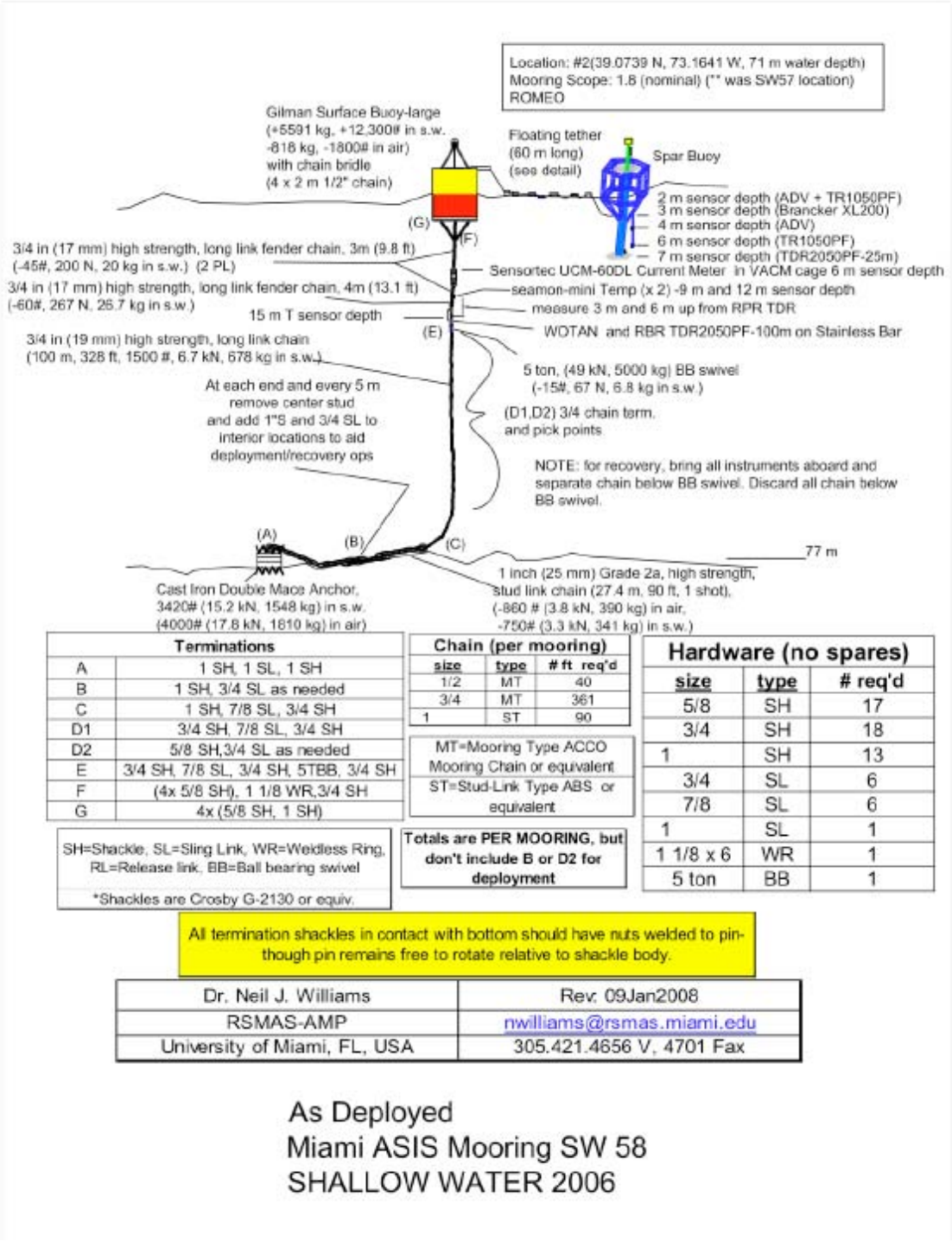

Figure 2.6 Sketch of an ASIS buoy attached with a tether buoy (Newhall et al., 2007).

2.3 Other Datasets

2.3.1 CTD Cast

During the experiment, CTD casts were conducted by several research vessels at well-defined locations and times (Figure 2.7). CTD data were recorded at a frequency of 24Hz. Suitable CTD profiles were used to estimate environmental parameters for our radar model simulations.

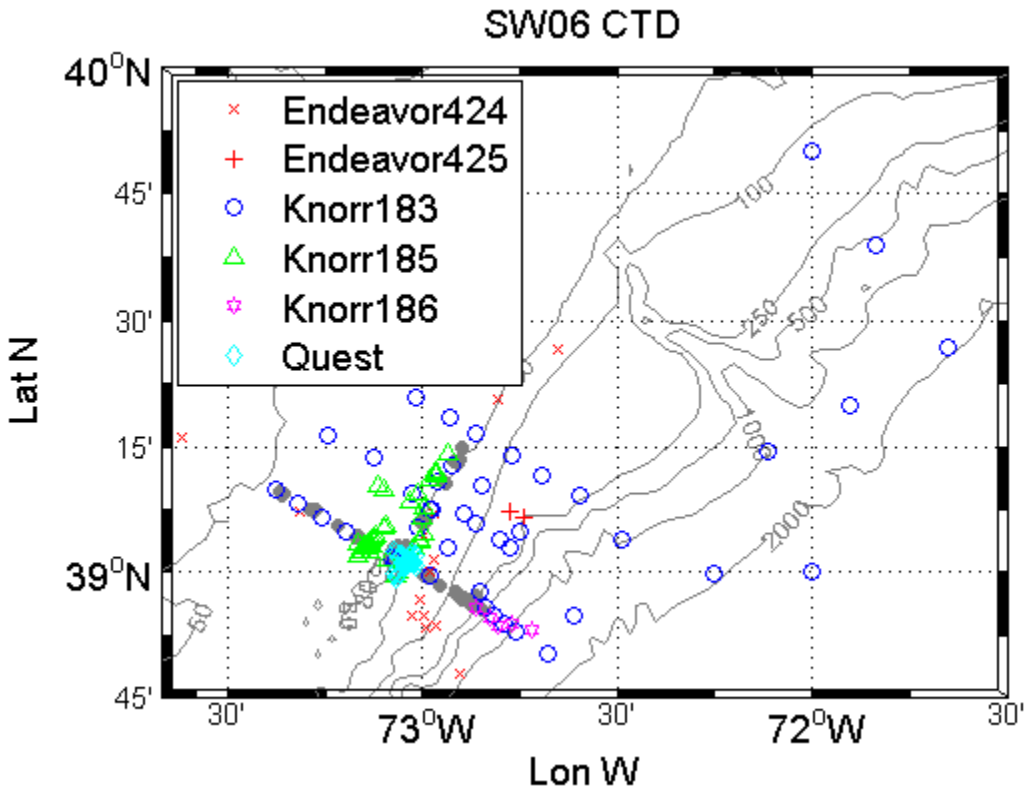

Figure 2.7 CTD distribution map of different research vessels in the SW06 experiment (Newhall et al., 2007).

2.3.2 BlendQscat Data

A surface wind dataset called BlendQscat has been derived from spatial blending of high-resolution satellite data (Seawinds instrument on the QuikSCAT satellite - QSCAT) and global weather center re-analyses (NCEP), resulting in a high temporal and spatial resolution dataset. It has a 6-hour temporal resolution and $0.5^{\circ} \times 0.5^{\circ}$ spatial resolution. The product provides wind vector components *u* and *v* and wind stress curl. Details of the blending methodology can be found in Chin et al (1998).

BlendQscat wind data (downloaded from http://dss.ucar.edu/datasets/ds744.4/data) was used to estimate the wind speed in the SAR coverage area in the experiment and to examine the dependence of IW occurrence with the wind speed.

CHAPTER 3 METHODS

The methods used in this study can be categorized as three parts: SAR image analysis, radar imaging model simulation, and in-situ data analysis.

3.1 SAR Image Analysis

3.1.1 Relative Intensity Profiles

In order to identify the different types of IW signatures, first we need to measure the relative intensity profiles along the wave propagation direction with respect to the background intensity, defined as

$$\delta I / I_0 = (I - I_0) / I_0 \qquad (1)$$

I is the intensity within the IW field and I_0 is the intensity of the image background taken from a homogeneous area (da Silva, et al., 1998).

To obtain a meaningful measurement of intensity and reduce speckle to a negligible magnitude, it is necessary to average along the wave crest. In SAR images, IWs have different propagation directions which make automatic averaging difficult. The easiest solution is to cut every IW signature out of the whole image and to rotate it to the horizontal direction, then to do the averaging along the lines and columns of the rotated image.

Second, an S_m value is calculated for the leading wave in every IW packet, defined as the quotient between strengths of the positive and negative parts of the signature, and written as

$$S_m = \left| (I_{\max} - I_0) / (I_0 - I_{\min}) \right| \qquad (2)$$

where $I_{\max}$ and $I_{\min}$ are the maximum and minimum value of I across the IW signature. When the positive modulation depth is dominant, S_m >1. Oppositely, when the negative modulation depth is dominant, S_m <1.

Figure 3.1 shows an ENVISAT image and traces of visible IWs over the bathymetry on July 23, 2006. Most of the IW packets are parallel to the bathymetry. The red square stands for the subsection area of IW12 in Figure3.2.

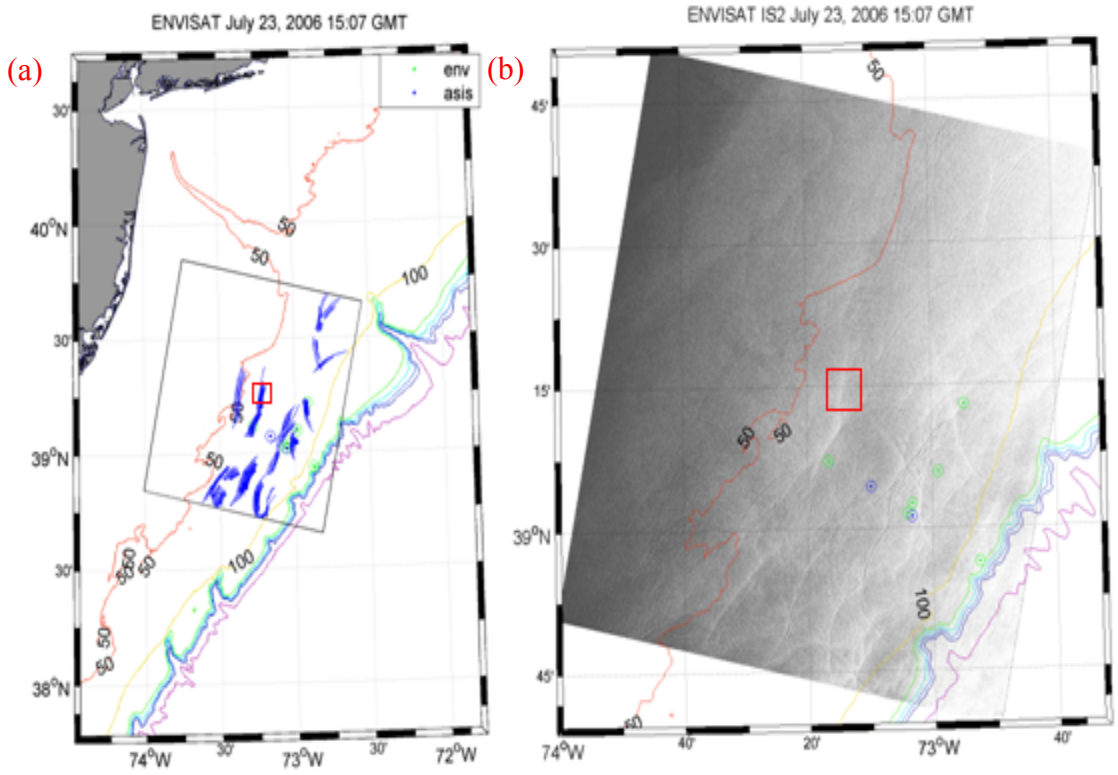

Figure 3.1 (a) Traces of IW packets in the ENVISAT image and (b) the ENVISAT ASAR image of July 23, 2006, over bathymetry. The red rectangle stands for the subsection area around IW12 in Figure 3.2.

Figure 3.2 gives an example of the whole process of calculating the relative intensity profile in the IW field. Figure 3.2(a) shows the subsection image of IW12 from the original SAR image, where the green rectangle stands for the background area (b) shows the image after rotating the IW12 crest parallel to the horizontal , where the red rectangle stands for the averaging area, and (c) shows the relative intensity profile of the IW12 field after averaging.

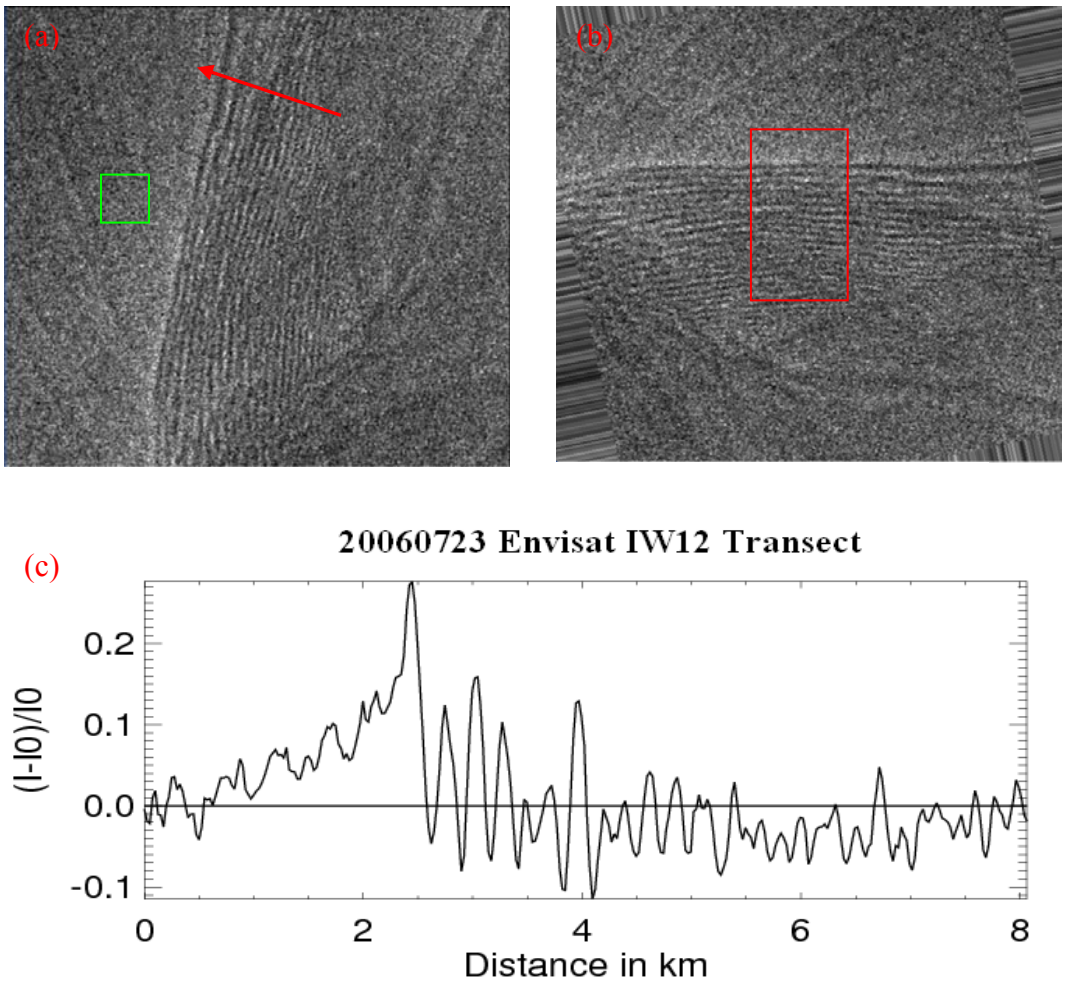

Figure 3.2 (a) The subsection of IW12 in the SAR image (b) IW12 wave crest parallel to the horizontal after rotation and (c) the relative intensity profile of the IW12 field after averaging along its wave crest.

3.1.2 IW Wavelength and Phase Velocity

The wavelength is defined as the separation between neighboring soliton intensity peaks. It can be calculated directly from the relative intensity profile of every IW packet.

Based on the assumption that an IW is induced by the tidal cycle, the phase velocity can be estimated using the separation distance between adjacent wave packets from the same generation location divided by the tidal period (Figure 3.3). In the MAB, the semidiurnal tidal component is dominant. Its period is about 12.4 h.

$$C = \frac{\Delta L}{\Delta T} \qquad (3)$$

C : IW phase velocity

ΔT : Tidal period (12.4 h)

ΔL : Distance separation between successive IW groups

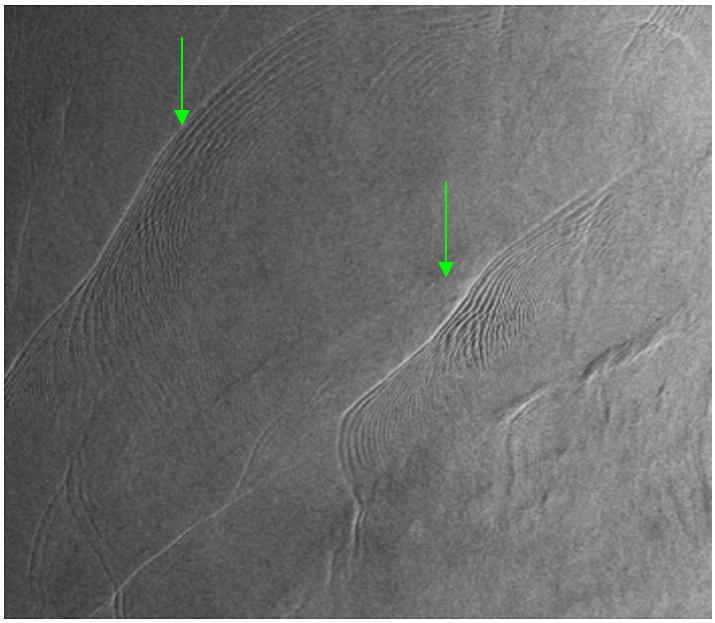

Figure 3.3 Two successive IW packets (green arrows) from the same generation location

Figure 3.3 shows an ideal situation. In some cases, we cannot find successive wave packets in a single SAR image or we cannot be sure about correct successive wave packet in a complex IW interaction area. Two sequential SAR images in a short time interval can be very helpful for phase velocity derivation in such situations. We can easily get the spatial distance shift in the wave propagation direction using a two-dimensional correlation method and calculate the wave velocity by knowing the time interval of the two images.

$$C' = \frac{\Delta l}{\Delta t} \tag{4}$$

C' : IW phase velocity

Δl : Distance shift between two images

Δt : Time interval between two images

In this experiment, ENVISAT IS2 beam mode has the same incidence angle as ERS2. They are almost in the same orbit with a temporal separation time interval of 28 minutes. Moreover, both of the images have a pixel resolution of about 25 m, a swath of 100 km, and Universal Transverse Mercator projection, which means the geo-location errors and pixel location errors are largely reduced (Zhao et al., 2008). In such situations, the upper bound of speed uncertainty is largely reduced. Thus these two kinds of images are well suited to be used together as sequential images to study the IW properties. In order to use cross correlation to derive the IW phase velocity, first we need to determine the exact same geo-location area for the feature we are interested in (Figure 3.4). The green line in Figure 3.4 shows the wave crest shift location in 28 minutes.

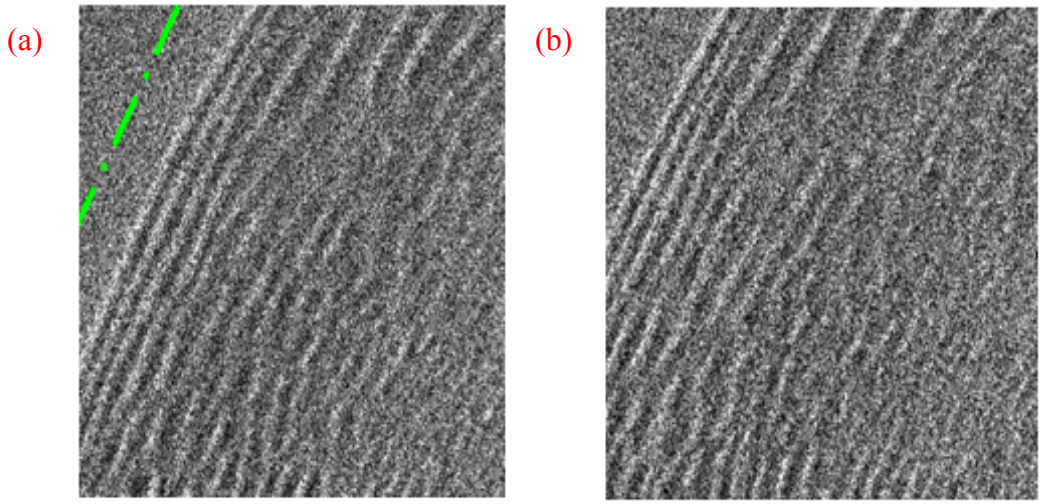

Figure 3.4 The same geo-location subsection from (a) ERS2 and (b) ENVISAT. The green line in (a) shows the leading wave crest location after 28 minutes.

3.2 Numerical Radar Signatures Simulation

A numerical radar imaging model is used to compute theoretical S_m values under different wind conditions and radar look directions. The model accounts for contributions of the full ocean wave spectrum to the radar backscatter from the ocean surface, based on resonant Bragg scattering theory in a composite surface model expansion. It includes additional terms accounting for the asymmetric distribution of scatters along intermediate scale surface waves due to hydrodynamic long wave-short wave interaction and the resulting upwind/downwind asymmetry of radar signatures. Details of the model can be found in the paper by Romeiser et al. (1994, 1997 a, b).

For the model, the mandatory input files define surface current and wind fields. The optional file used in this study is frame speed. For IW simulations, an additional inout file defines the frame speed of a moving frame of reference in which the current field is

quasi-stationary. This Frame speed is equal to the phase velocity of the IW. Using the frame speed file, the model integrations take place from a moving frame point of view; that is, the frame speed vector will be subtracted from each given current vector to account for the apparent mean current in the moving system.

For the model simulation, the surface current profile induced by IWs is estimated on a two-layer Korteweg-de Vries (KdV) equation:

$$\eta(x,t) = \mp\eta_0 \sec h^2\left[(x - C_p t)/l\right] \quad (5)$$

$$C_p = C_0[1 + \eta_0(h_2 - h_1)/(2h_1h_2)] \quad (6)$$

$$l = 2h_1h_2 / \sqrt{3\eta_0|h_2 - h_1|} \quad (7)$$

$$C_0 = \sqrt{g\Delta\rho h_1 h_2 / \rho(h_1 + h_2)} \quad (8)$$

η_0 : IW amplitude;

h_1 : Mixed layer depth ;

h_2 : Bottom layer thickness;

C_p : Nonlinear IW phase velocity.

C_0 : The linear wave speed

g : The gravity acceleration

ρ : The density of the water

$\Delta\rho = \rho_2 - \rho_1$: the density differences between two layers

The horizontal velocity of surface current induced by IWs:

$$U_x = \pm\frac{C_0\eta_0}{h_1}\sec h^2\left[(x - C_p t)/l\right] \quad (9)$$

where C_p is used as the frame speed.

Besides the three input files, we need to specify radar frequency, radar polarization, incidence angle and radar look direction to run the radar signature simulation. Figure 3.5 gives an example of an NRCS profile simulated by the model. We can determine $I_{\max}, I_{\min}, I$ from the profile and calculate the corresponding S_m value.

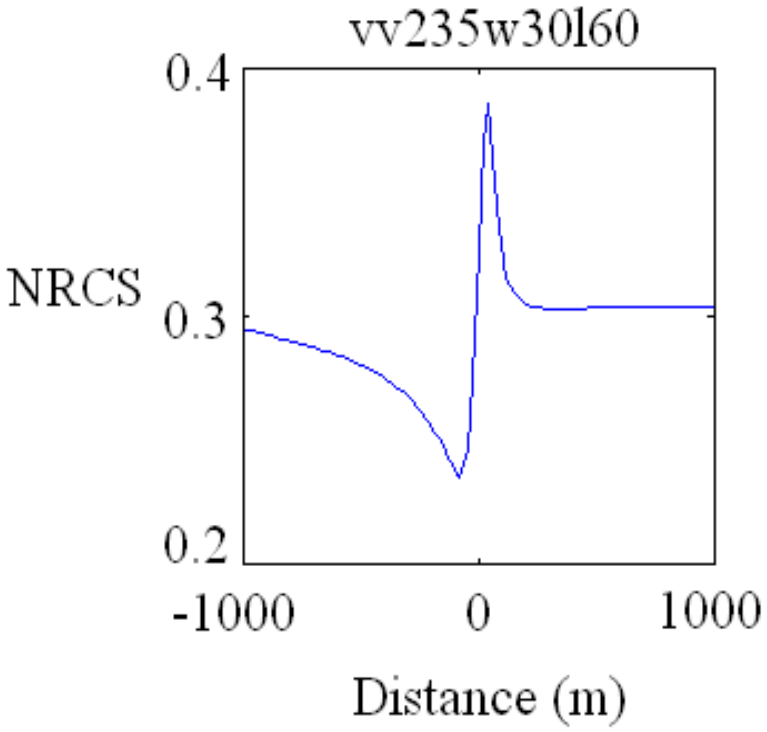

Figure 3.5 NRCS variation along an IW field when the wind speed is 5 m/s, $\theta_{Wind-IW}$ is 30° and $\theta_{Look-IW}$ is 60°.

3.3 In-Situ Data Analysis

For ADCP data, first a 4th-order high pass filter with a cutoff frequency at 0.0042 cycles per day, or 4 hours, is used to remove wind and tidal oscillations from the time series. Second, the axial horizontal current in the IW propagation direction is calculated.

$$U = -u\sin\theta + v\cos\theta \qquad (10)$$

where θ is the angle between IW propagation direction and the north direction. u and v are the current velocities in the east and north direction measured by the ADCP (Figure 3.6).

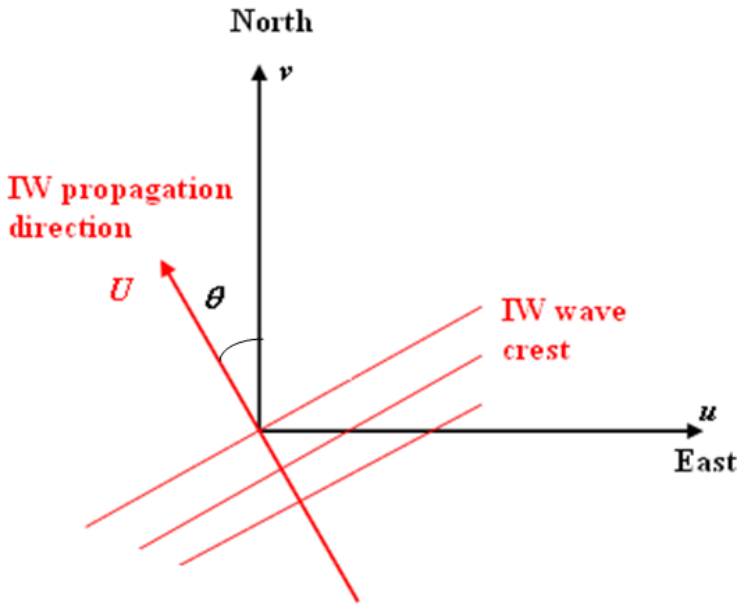

Figure 3.6 Projection of an earth-referenced current velocity coordinate to the axial horizontal current in IW propagation direction.

For CTD profiles, the data in the first several meters are discarded due to the CTD instability. The remaining data is smoothed (i.e., 10 points smoothing) and interpolated every 0.5 m. Density profiles and the Brunt-Vaisala frequency, or stability frequency

profile can be plotted. The depth of maximum Brunt-Vaisala frequency is an approximation of the mixed layer depth, and the reduced gravity can be estimated based on the two-layer model.

CHAPTER 4 RESULTS

Three main results are presented in this chapter. The first part is about the relationship between IW signature occurrence in SAR images and wind speed. The second part shows the statistical finding about the relationship between S_m values and $\theta_{Wind-IW}$ for all leading IWs in the SAR images. The last part studies an IW interaction case by using two sequential SAR images with a time interval of 28 minutes and in-situ measurements near the interaction pattern.

4.1 IW Occurrence Versus Wind Speed

The number of observed IW packets in each SAR image has been counted. There are 331 IW packets in total in 57 SAR images. Since the ASIS buoys only worked from August 2 to September 6, 2006, the wind speed in every image has been estimated from the BlendQscat wind data instead of ASIS buoy wind data.

Figure 4.1 shows that the occurrence of IW signatures is highly dependent on the wind speed. The left axis is number of IW observed in total for different wind speed and the right axis is number of IW observed per image we collected for different wind speed. It can be found that it is hard to observe IW signatures in SAR images when the wind speed is higher than 10 m/s or lower than 2 m/s. In contrast, the moderate wind speeds from 4-7 m/s are most favorable for imaging IW signatures. The result agrees well with the statistic results obtained from the northern South China Sea (Huang et al., 2009), where high winds and very low winds were found to be unfavorable for SAR imaging of IWs.

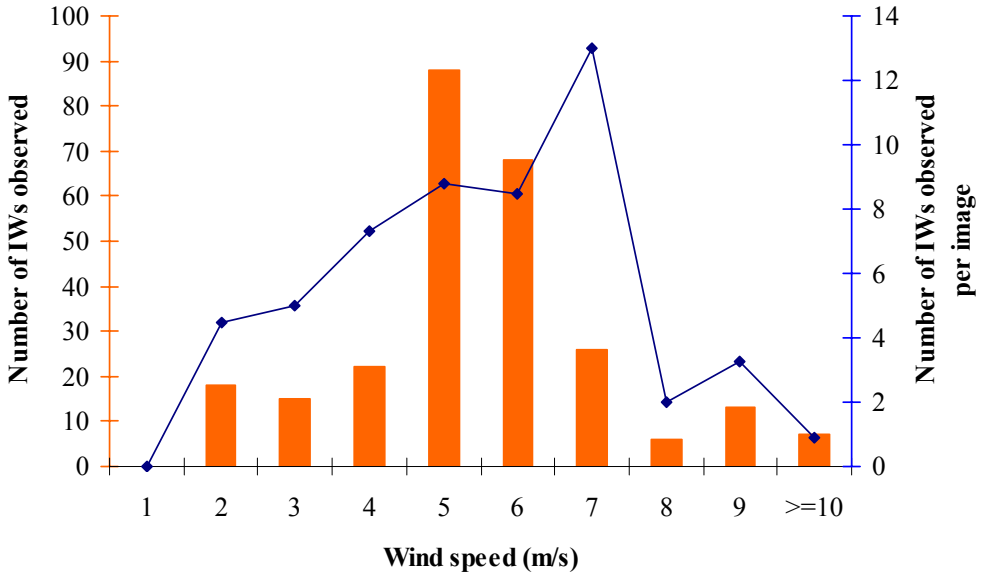

Figure 4.1 IW signature occurrences in SAR images versus wind speed

4.2 S_m Value Versus $\theta_{Wind-IW}$

The relative intensity profiles of 331 IW signatures from all 57 SAR images have been analyzed and the corresponding S_m values for leading IW in every packet have been calculated. Figures 4.2, 4.3 and 4.4 give examples showing the three different types of IW signatures in SAR images in the experiment (single positive, double sign, single negative) and their characteristic backscatter modulation intensity profiles. These three examples are not affected by atmospheric or surface film effects.

Spatial variations of the wind field due to the atmospheric effects, which can lead to an extraordinary dark or bright background, can result in different signature types. Figures 4.5 and 4.6 show two examples of single positive and single negative IW signatures due to the atmospheric effects.

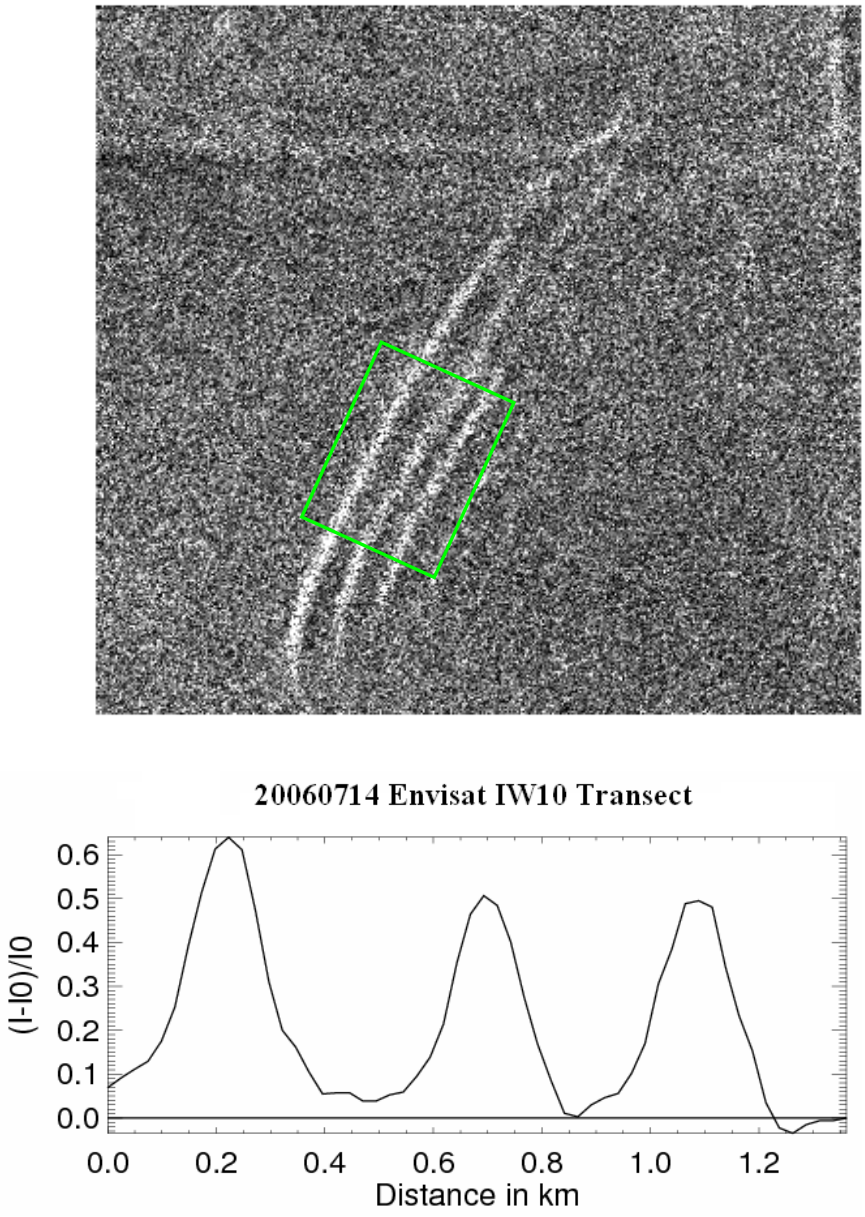

Figure 4.2 A single positive IW signature and its backscatter intensity modulation profile. The green box shows the averaging area.

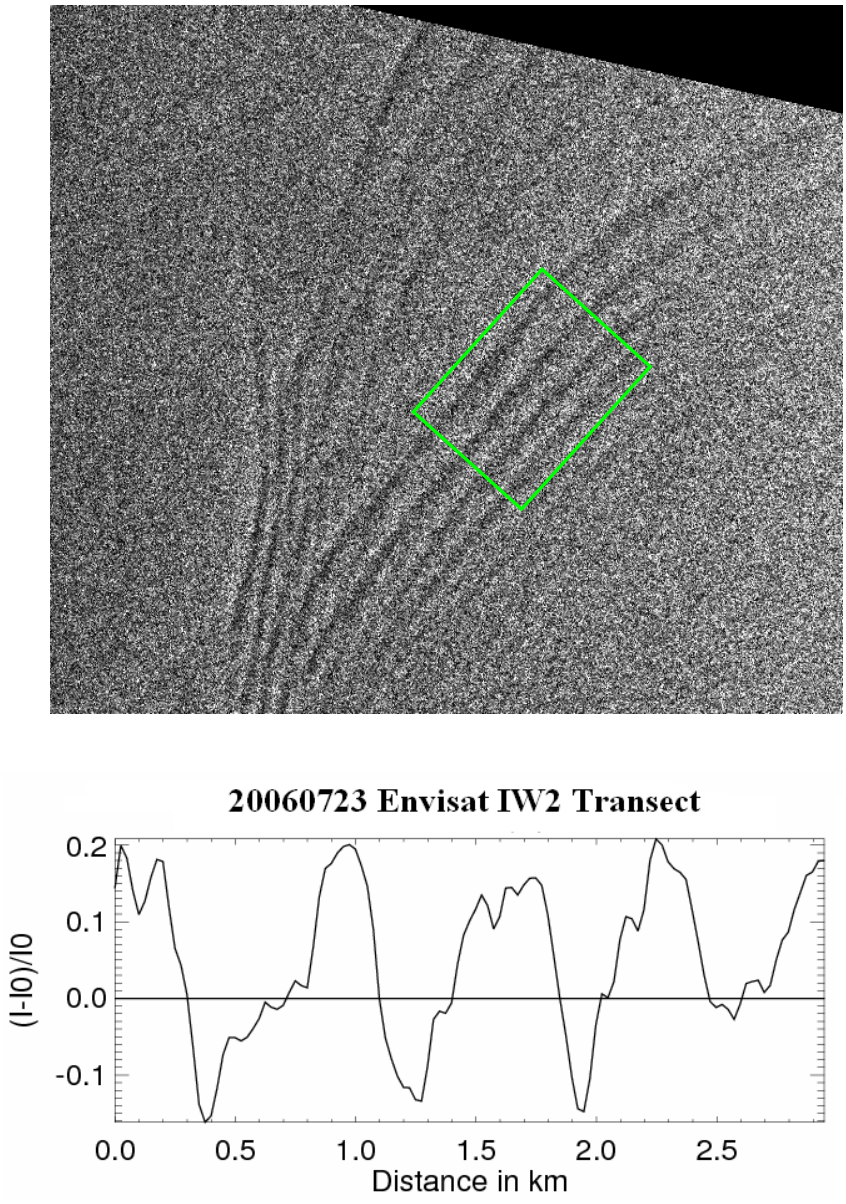

Figure 4.3 A double sign IW signature and its backscatter intensity modulation profile. The green box shows the averaging area.

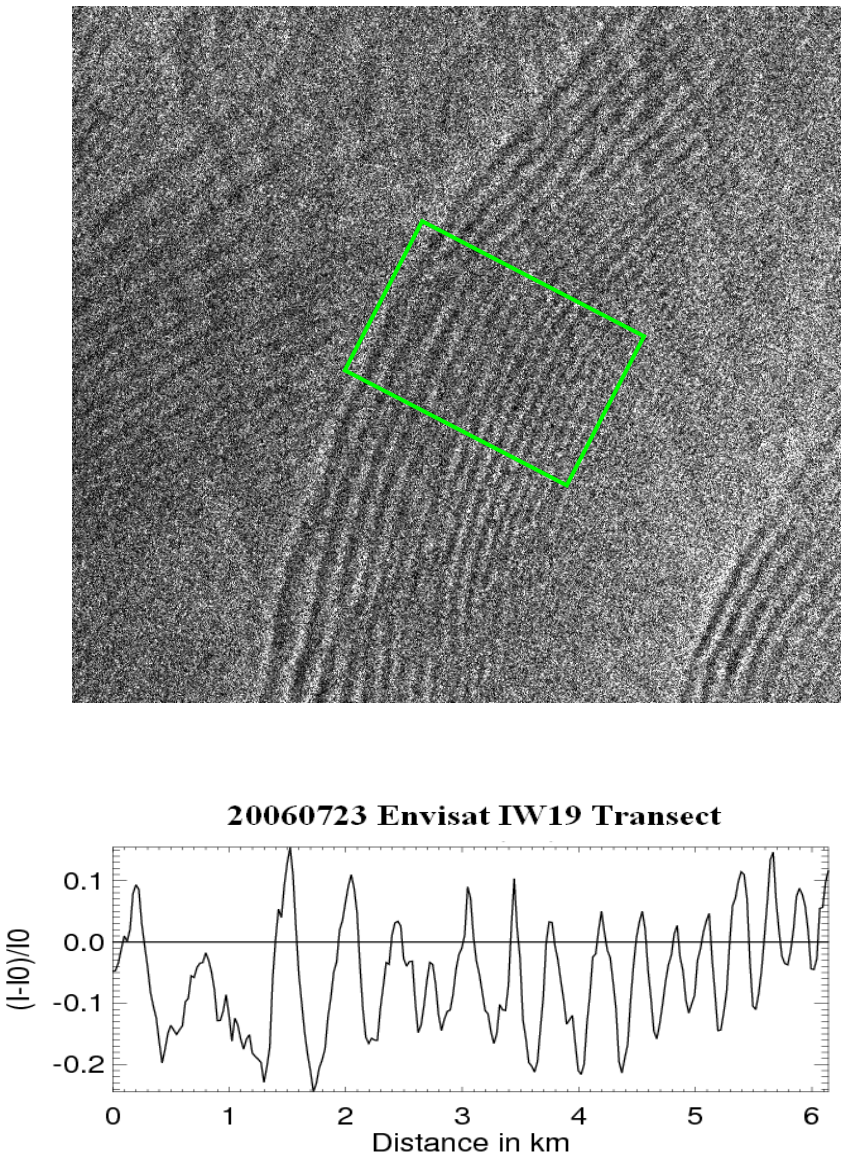

Figure 4.4 A dominantly negative of IW signature and its backscatter intensity modulation profile. The green box shows the averaging area.

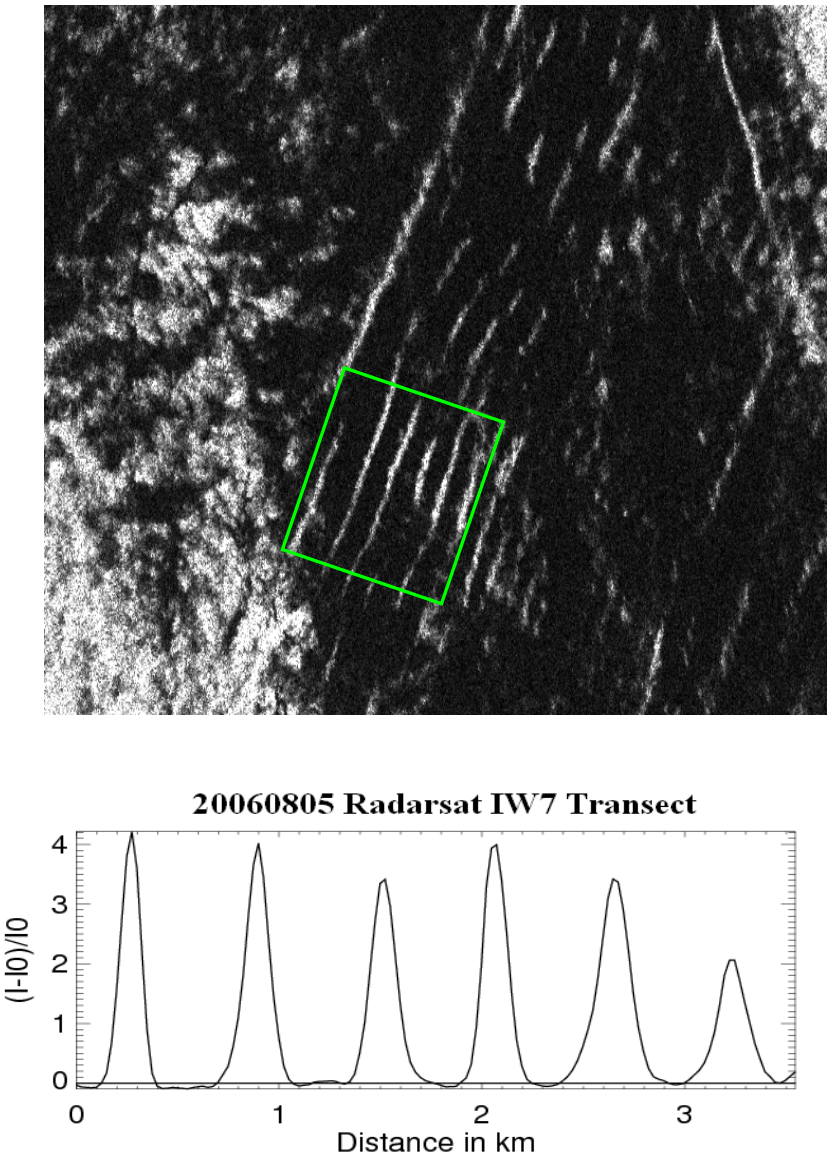

Figure 4.5 A single positive IW signature in the presence of strong atmospheric features and its backscatter intensity modulation profile. The green box shows the averaging area.

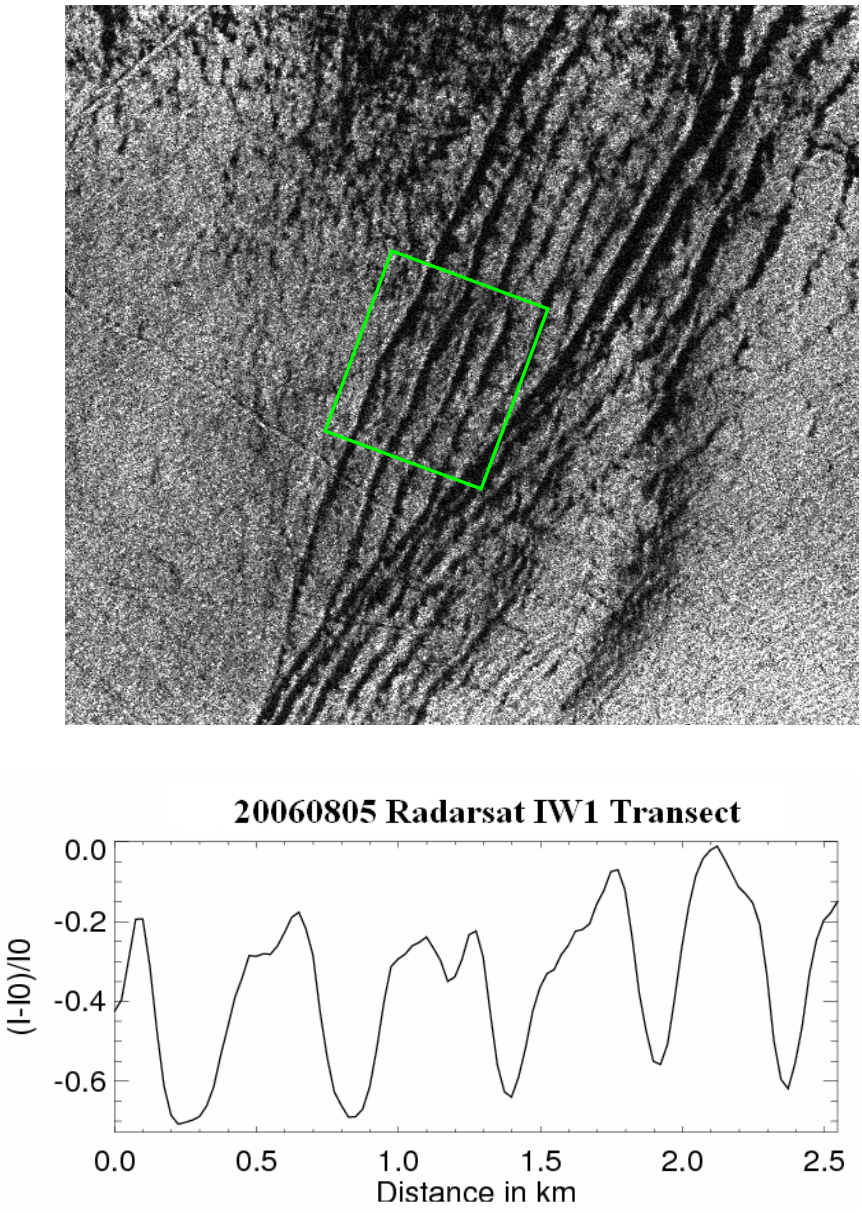

Figure 4.6 A single negative IW signature due to the atmospheric effect and its backscatter intensity modulation profile. The green box shows the averaging area.

The other possible cause in the literature for different IW signature types is different $\theta_{Wind-IW}$. Da Silva et al. (2002) examined the role of wind direction on SAR signature types in the western Iberian shelf and suggested that IWs propagating against the wind direction were primarily imaged mostly as positive signatures, while those propagating in the wind direction were mostly negative sign signatures. In the MAB, similar statistics can be done to examine the relationship between the signature types and the angle between IW propagation and wind direction.

In this study, the local wind conditions were measured by ASIS buoys, which were operational from August 2 to September 6, 2006. Therefore, only images in this period have been used in the statistics. Moreover, only ENVISAT and RADARSAT images were used to alleviate duplicate counts between ENVISAT and ERS2, which almost have the same IW signatures due to their short time lag and similar radar parameters. Last but not least, all IW signature affected by atmospheric effects are excluded.

Table 4.1 gives details of the wind direction and speed from the two ASIS buoys during SAR imaging times. The wind direction used in the statistics is the average of the two buoys results. The propagation direction of every IW can be measured from images directly, then $\theta_{Wind-IW}$ can be calculated. Figure 4.7 shows the relationship between S_m and $\theta_{Wind-IW}$ where the red line represents the IW double signature (S_m=1). Most of the S_m values are large than 1, which means positive signatures are prevailing, when $\theta_{Wind-IW}$ is less than 90°. In contrast, the results from da Silva et al. (2002) showed most of the S_m values being less than 1, which means negative signatures were prevailing, when $\theta_{Wind-IW}$ was less than 90°.

Satellite	Imaging time	Direction (Romeo)	Speed (Romeo)	Direction (Yankee)	Speed (Yankee)
ENVISAT	8/2/2006 2:28	213.0	2.9	266.0	5.2
ENVISAT	8/8/2006 15:00	354.0	6.8	347.3	7.5
ENVISAT	8/18/2006 2:37	66.5	7.2	98.7	8.3
ENVISAT	8/27/2006 15:07	150.0	10.4	157.2	9.6
ENVISAT	9/3/2006 3:03	247.0	1.1	298.0	2.7
ENVISAT	9/6/2006 2:40	238.0	6.5	252.0	9.4
RADARSAT	8/1/2006 22:42	209.0	1.6	259.0	6.0
RADARSAT	8/5/2006 22:37	22.8	2.6	21.1	3.2
RADARSAT	8/6/2006 10:51	72.0	5.3	45.3	4.5
RADARSAT	8/8/2006 22:38	13.7	6.1	12.2	6.2
RADARSAT	8/9/2006 11:03	37.5	6.3	63.2	7.8
RADARSAT	8/12/2006 22:33	349.6	2.5	4.5	4.6
RADARSAT	8/13/2006 10:47	353.0	6.3	359.0	7.4
RADARSAT	8/15/2006 22:45	242.0	8.4	240.0	7.6
RADARSAT	8/16/2006 10:59	124.0	8.4	123.0	9.3
RADARSAT	8/18/2006 22:58	105.0	5.1	98.0	6.2
RADARSAT	8/20/2006 10:43	225.0	11.0	223.3	11.8
RADARSAT	8/22/2006 22:41	173.0	3.05	218.0	3.1
RADARSAT	8/23/2006 10:55	260.0	3.4	250.7	4.0
RADARSAT	8/25/2006 22:54	260.0	7.7	260.0	8.3
RADARSAT	8/29/2006 22:37	146.0	4.0	100.0	1.4
RADARSAT	8/30/2006 10:51	67.6	10.5	52.5	11.3
RADARSAT	9/1/2006 22:50	90.8	18.8	83.8	19.6
RADARSAT	9/2/2006 11:04	108.9	20.6	111.6	20.9
RADARSAT	9/5/2006 22:33	131.0	13.3	147.0	11.3
RADARSAT	9/6/2006 10:47	14.0	7.7	17.7	8.9

Table 4.1 Wind direction and speed from two ASIS buoys at SAR imaging times.

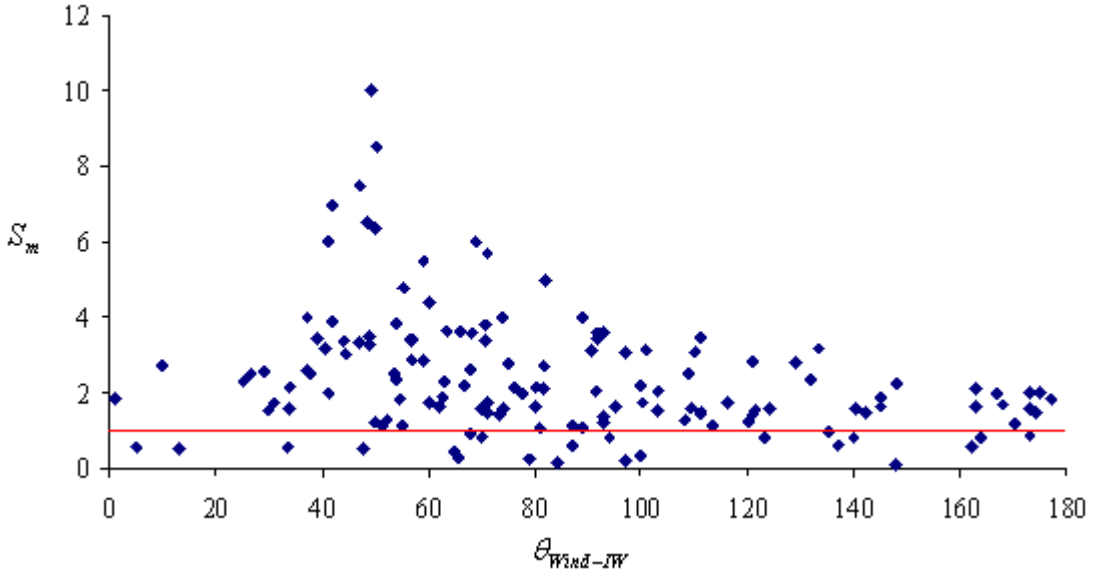

Figure 4.7 S_m versus $\theta_{Wind-IW}$. The red line stands for IW double sign signature (maximum positive modulation equal to maximum negative modulation).

4.3 IW Interaction Case Study

Clear IW interaction patterns are hard to observe in SAR images. Luckily, there is a good IW interaction case in the SW06 dataset. The distinct X pattern is shown on two sequential SAR images with a 28 minutes time interval on August 08, 2006. Moreover, the moorings SW32, SW33 and SW19 are on the both sides of the pattern.

Figure 4.9 (a) and (b) shows this X pattern in the ENVISAT and ERS2 image respectively. Four IW groups in this pattern are labeled as IW1a, IW1b, IW2a and IW2b. Note that the terms IW1a and IW1b, as well as IW2a and IW2b, are used to indicate the same wave group.

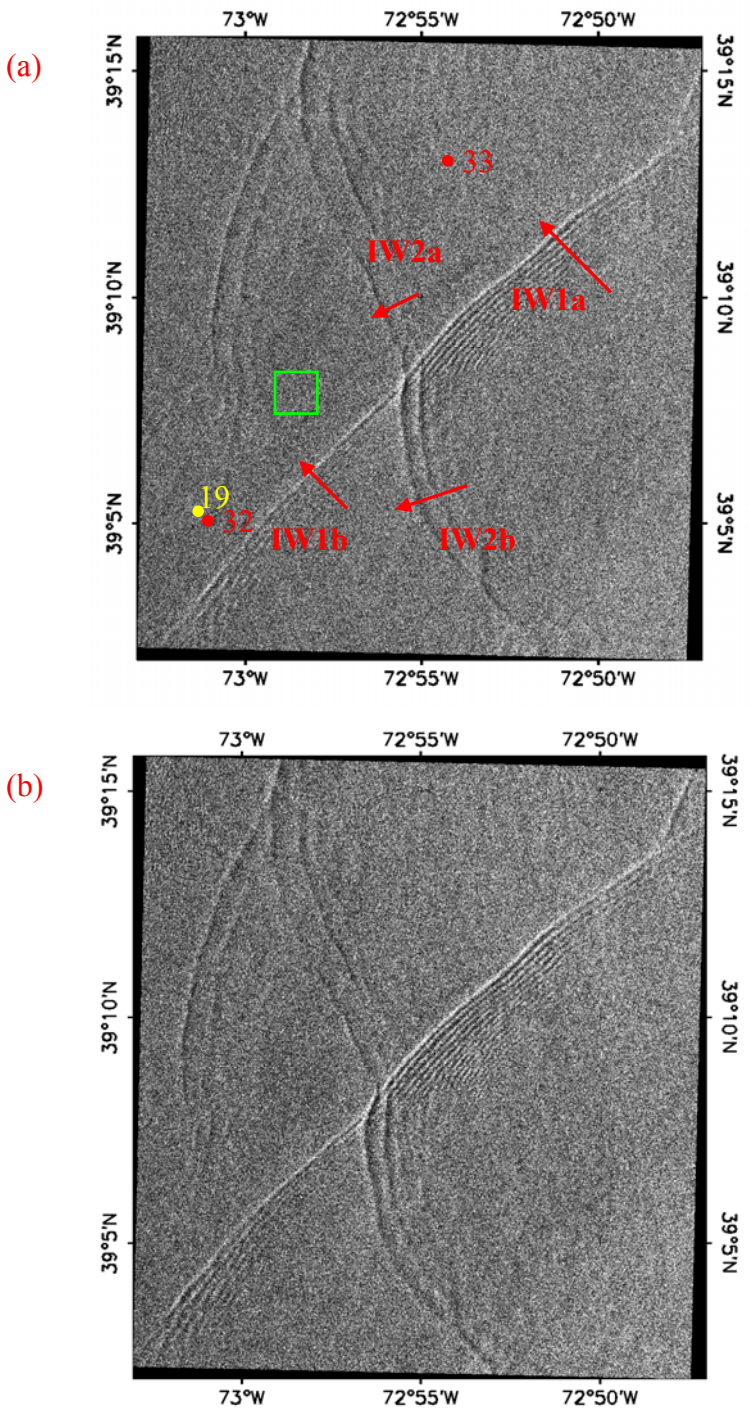

Figure 4.8 (a) The IW interaction pattern in the ENVISAT image taken at 15:00 UTC on August 8, 2006. Moorings SW32, SW33 are shown as red dots and SW19 is shown as a yellow dot. The red arrows stand for IW1a, IW1b, IW2a and IW2b and represent four parts of the interaction pattern. The green box is the area used for determining image background intensity. (b) The same IW interaction pattern in the ERS2 image taken at 15:28 UTC on August 8, 2006.

SW32 (72.99 ° E, 39.10 ° N) at 80 m water depth and SW33 (72.91 ° E, 39.20 ° N) at 81 m water depth marked as red dots are located on the two sides of the interaction pattern. SW19 (73.01 ° E, 39.10 ° N) is near SW32 at a water depth of 79 m and is marked as a yellow dot. The green box is the area used for determining image background intensity.

Figure 4.9 shows relative intensity profiles of the four parts. First, we can clearly see that IW1a has a relatively stronger signature than IW1b. IW1a has a positive modulation around 0.52 of the leading wave and 0.27 for the rear ones, while IW1b has 0.41 for the leading IW and 0.15 for the rear ones. Similarly, IW2b has a stronger signature than IW2a. IW2a has a positive modulation of the leading wave around 0.28 while IW2b has 0.15. The intensity difference may imply an energy exchange between the two IW groups due to the interaction. Explicitly, IW1 gains energy while IW2 loses energy due to the interaction. It is a good guess that IW1b and IW2b are before-interaction pair while IW1a and IW2a are after-interaction pair. Second, IW1b has a stronger intensity than IW2b. From the simulation of Yang et al., 2000, the larger positive modulation is related to a larger amplitude assuming that other parameters are similar. This implies that the amplitude of IW1 is larger than IW2.

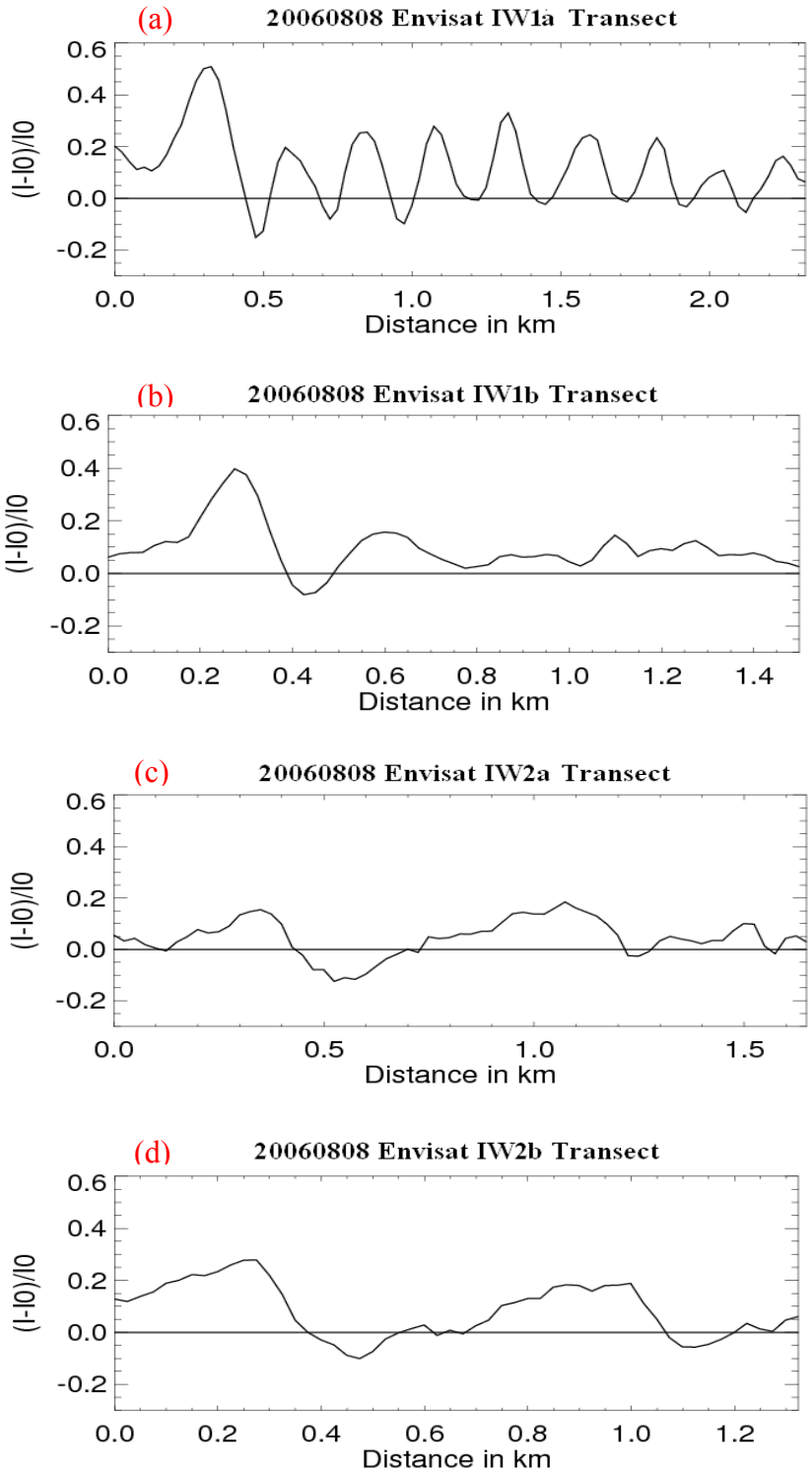

Figure 4.9 Relative intensity transects of (a) IW1a, (b) IW1b, (c) IW2a and (d) IW2b. The straight black lines show background intensity.

Phase velocities for the interaction pattern can be derived by cross correlation. The four parts of the pattern were cropped off separately in order to use the method. The results show that IW2 has a large phase velocity change from 0.94 m/s to 0.65 m/s after interaction while the IW1 velocity does not change much (Table 4.2). The large velocity change in IW2 explains the distortion in the interaction part after 28 minutes in the ERS2 image (Figure 4.9).

ID	IW1a	IW1b	IW2a	IW2b
C (m/s)	0.46	0.59	0.65	0.94

Table 4.2 Phase velocities of the interaction pattern derived from two sequential SAR images.

SW32 and SW33 are on the two sides of the pattern, providing temperature and current records for a better understanding of the interaction process. The temperature sensors on the moorings can record the disturbances within the water column during the IW passings and indicate the wave amplitudes. Unfortunately, SW32 had errors in the temperature record. Therefore the temperature record from SW19 was used. Figure 4.10 shows the temperature records when the IWs were passing the moorings. The temperature disturbance generated by IW2a and IW2b is too weak to be detected in the moorings. The amplitudes are at most 3 m assuming the IW generation depth is around 10 m. Clearly IW1a and IW1b generate much stronger temperature disturbances than IW2a and IW2b, which imply much larger amplitudes. However, the amplitudes cannot be estimated accurately due to the 10 m vertical resolution and no temperature data collected near the surface.

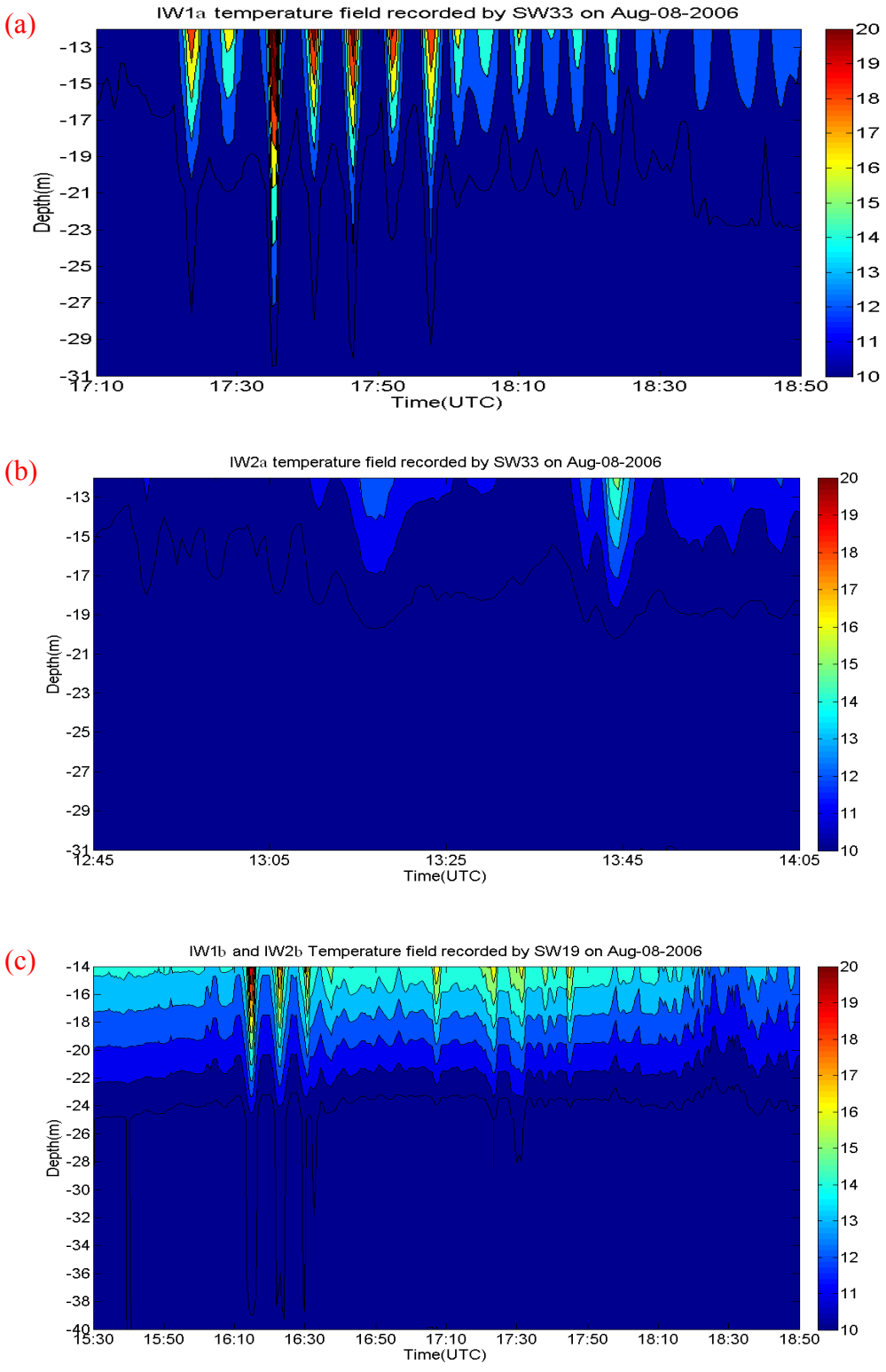

Figure 4.10 (a) Temperature profile when IW1a is passing SW33. (b) Temperature profile when IW2a is passing SW33. (c) Temperature profile when IW1b and 2b are passing SW19.

Current field disturbance is also a good sign for IW passage. SW32 and SW33 both had an ADCP mounted near the bottom with 4 m bins and a 30 second sampling period. Figures 4.11 and 4.12 show the ADCP velocity data for the pairs before interaction and after interaction. The red line is the vertical velocity with a mean of zero which is very sensitive to IW passages. There is a very strong vertical velocity oscillation during the IW1a and IW1b passage, while a very weak disturbance occurs during IW2a and IW2b passage, which is consisted with the temperature profile observation. The green line and the blue line are reoriented horizontal velocities at two water depths. For IW1a and IW1b, the horizontal velocity is also showing the strong signature of the IW passing. For IW2a and IW2b, the horizontal velocity in shallow water depth shows much stronger signatures than the vertical velocity.

Overall, the current velocity data shows much clearer signatures of IWs passing than the temperature data. We can use the start point of the velocity oscillation to estimate the time at which the IWs arrived at the moorings. The local IW phase velocity can be estimated based on the distance and time separation between mooring location and IW location in the SAR imagery. For example, a wave velocity of IW1b of 0.54 m/s can be estimated from the 1.4 km distance between the mooring location and the wave front in the SAR image and the 43 minutes time lag between the SAR imaging time and the IW arrival time.

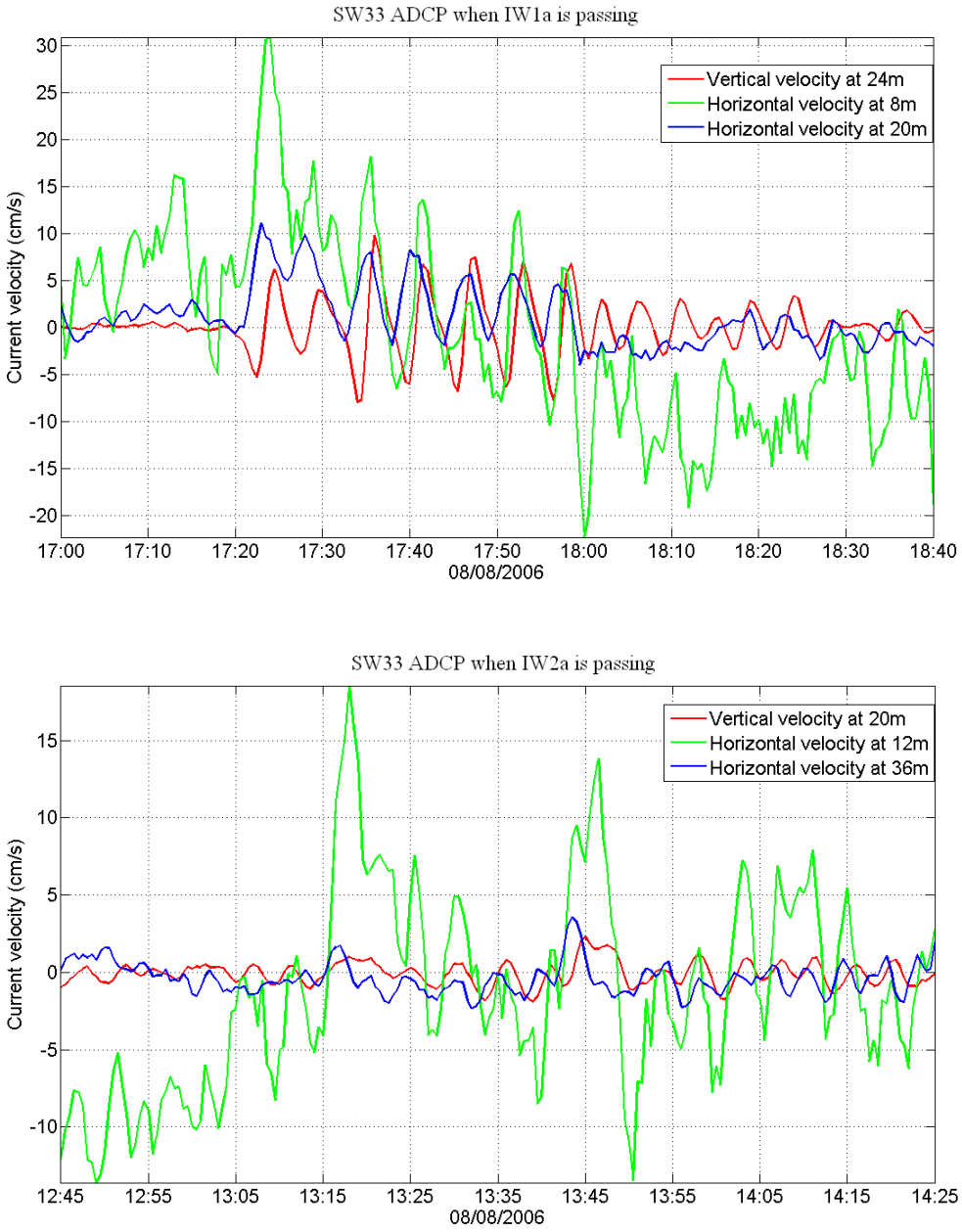

Figure 4.11 (a) Vertical velocity at 24 m (red), horizontal velocity at 8 m (green) and at 20 m (blue) at SW33 when IW1a is passing on Aug 08, 2006 (b) Vertical velocity at 20 m (red), horizontal velocity at 12 m (green) and at 36 m (blue) at SW33 when IW2a is passing on Aug 08, 2006.

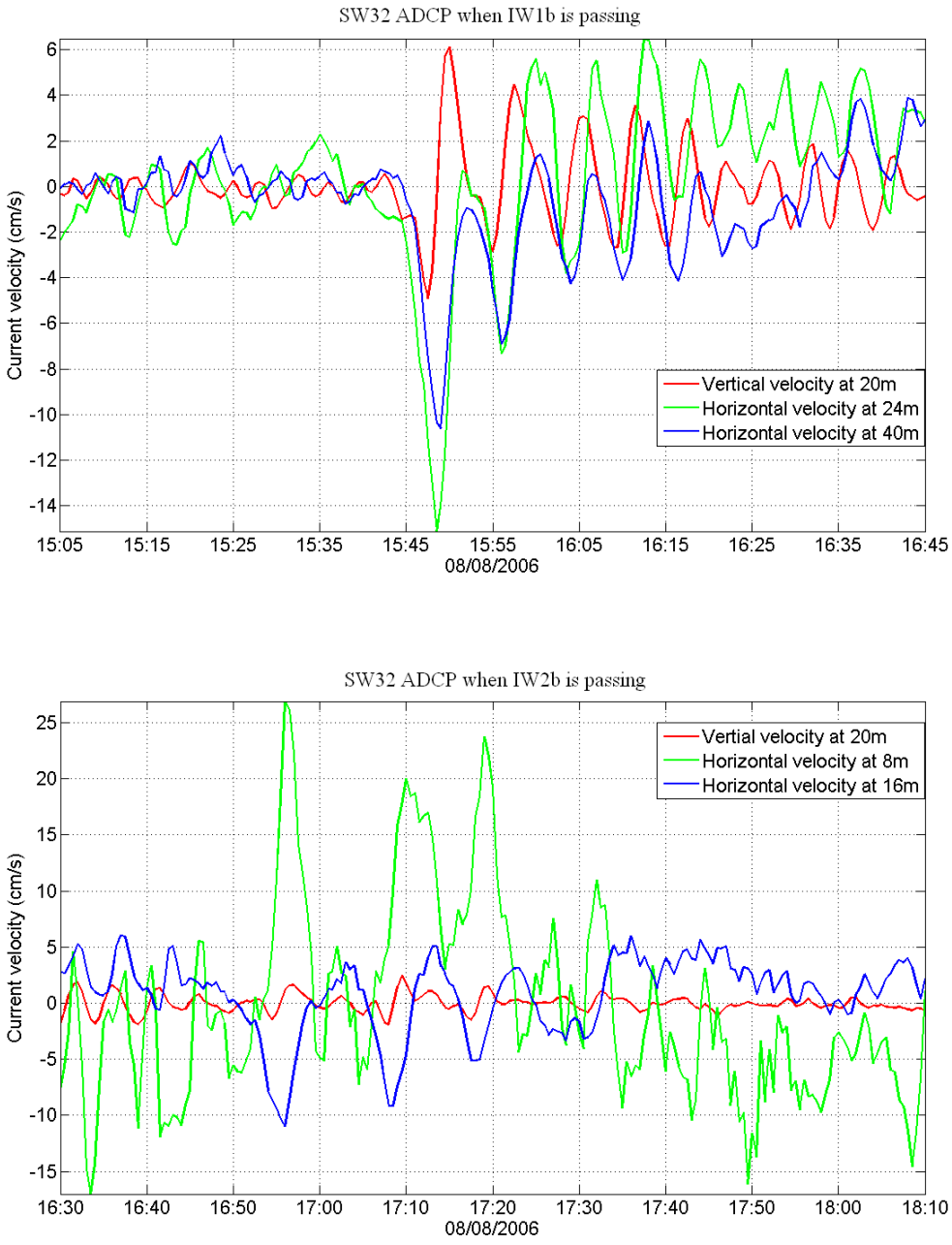

Figure 4.12 (a) Vertical velocity at 20 m (red), horizontal velocity at 24 m (green) and at 40 m (blue) at SW32 when IW1b is passing on Aug 08, 2006. (b) Vertical velocity at 20 m (red), horizontal velocity at 8 m (green) and at 16 m (blue) at SW32 when IW2b is passing on Aug 08, 2006.

Table 4.3 shows IW phase velocities of the four parts derived from the ENVISAT image and the current record. The same analysis from the ERS2 image and moorings are also done. Figure 4.13 shows the phase velocity differences obtained by the three different methods (ENVISAT-ERS2, ENVISAT-EM, ERS2-EM). EM denotes environmental mooring. The results of the three different methods are in good agreement except for IW1b. The small distance between the mooring and the IW1b front in the SAR image may be responsible for such poor agreement, because even two pixels bias in the distance measurement can result in a large phase velocity bias. For the ERS2 and mooring combination, the largest uncertainty bias also comes from the small time lag between the IW1b mooring arrival time and SAR imaging time.

ENVISAT	IW1a	IW1b	IW2a	IW2b
Arriving time (hh:mm)	17:22	15:43	13:14	16:54
Time interval (minutes)	142	43	106	114
Distance (km)	4.36	1.40	4.84	6.42
Phase velocity (m/s)	0.51	0.54	0.65	0.94

Table 4.3 Phase velocities of the interaction pattern derived from the moorings and the SAR images.

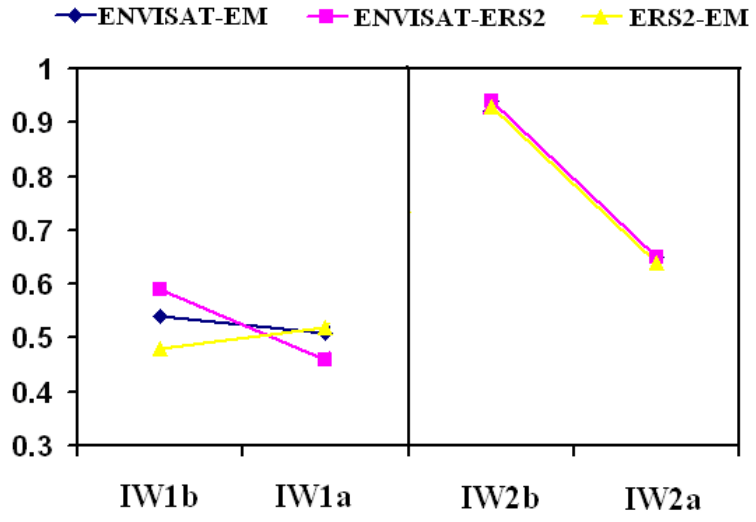

Figure 4.13 Comparisons of phase velocities from the different methods.

CHAPTER 5 DISCUSSION

5.1 Wind Dependence of IW SAR Signatures

Figure 5.1 shows the relationship between S_m and $\theta_{Wind-IW}$ for ERS images of the Iberian shelf from da Silva et al. (2002). S_m values increase with $\theta_{Wind-IW}$. In addition, most of S_m value are less than 1 when $\theta_{Wind-IW}$ is less than 90° while most S_m values are large than 1 when the angle is larger than 90°. Da Silva et al. (2002) suggested that IWs propagating against the wind direction are primarily imaged as positive sign signatures, while those propagating in the wind direction are mostly negative sign signatures. This could be explained by using a wind contrast model based on simple first-order Bragg scattering theory and hydrodynamic wave-current interaction theory (Figure 5.2). The model results agreed well with the observations.

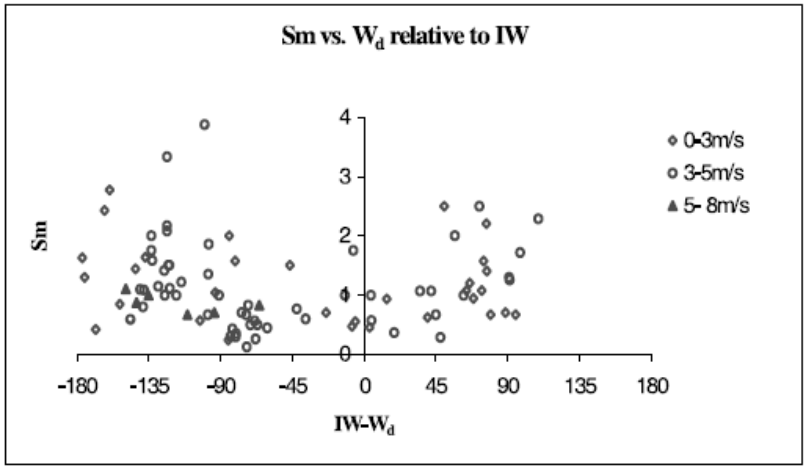

Figure 5.1 S_m versus $\theta_{Wind-IW}$ for ERS images of the Iberian shelf. (da Silva et al., 2002)

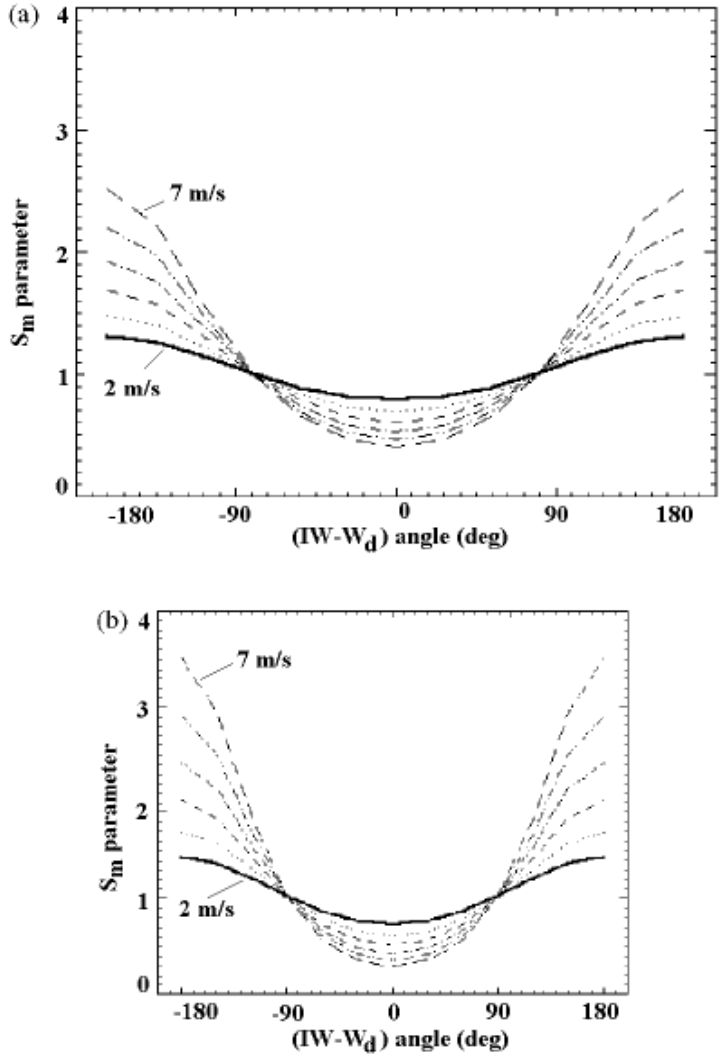

Figure 5.2 Model results for two different angles between the radar look direction and the IW propagation direction, (a) for $\varphi = 0°$ (b) for $\varphi = 30°$ showing the dependence of S_m on the angles between IW propagation direction and wind direction. Different curves in each plot correspond to different wind velocities, starting from $2\,\mathrm{ms}^{-1}$ for the continuous dark line and increasing to $7\,\mathrm{ms}^{-1}$ (da Silva et al., 2002).

In this study, statistics in the MAB (Figure 4.7) show a different behavior than the result of da Silva et al. (2002): most S_m values larger than 1 when $\theta_{Wind-IW}$ is less than 90°. We have tried to use the radar imaging model described in 3.2 to investigate this in more details. The surface current profile induced by IWs in the model is based on the two-layer KdV equation. The CTD profile of Endeavor 424 03 (72.98° W, 39.00° N) on Aug 5, 2006 has been used to represent the conditions in the water. Figure 5.3 shows the buoyancy frequency profile and density profiles, which give an estimate of h_1=12 m, h_2 =68 m, $\Delta\rho = \rho_2 - \rho_1$ =1026-1020 =6 kg/m^3 and ρ = (1026+1020)/2 =1023 kg/m^3. C_p =0.8183 ms^{-1} can be calculated by using equation (2). Assuming IW amplitude of 5 m, the current profile according to equation (5) is shown in Figure 5.4.

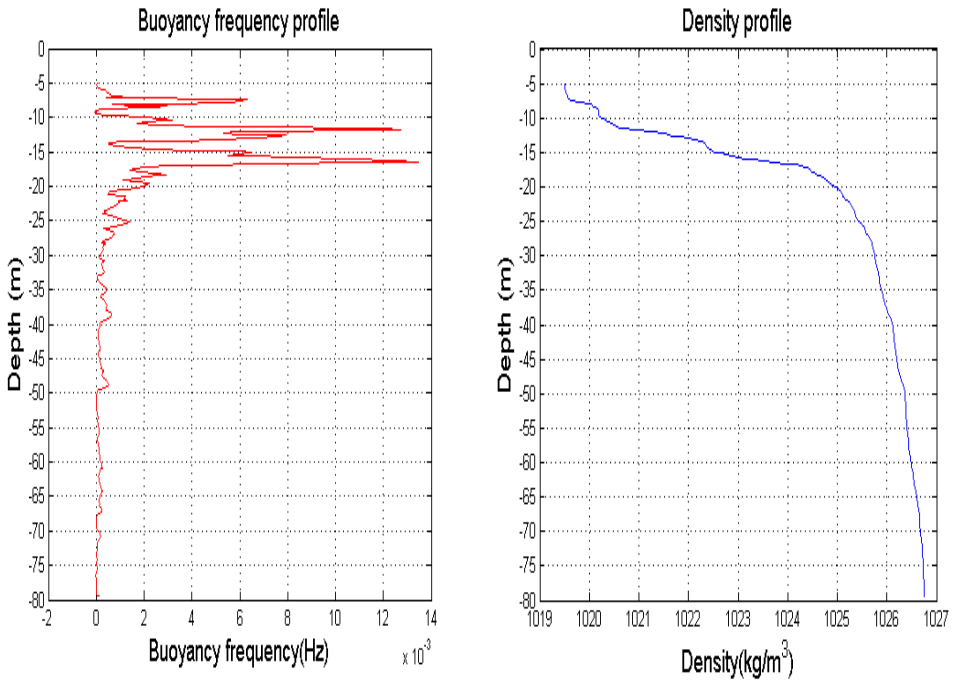

Figure 5.3 Buoyancy frequency and density profile from the Endeavor 424 CTD cast 03 (72.98° W, 39.00° N) in a water depth of 80 m on Aug 05, 2006.

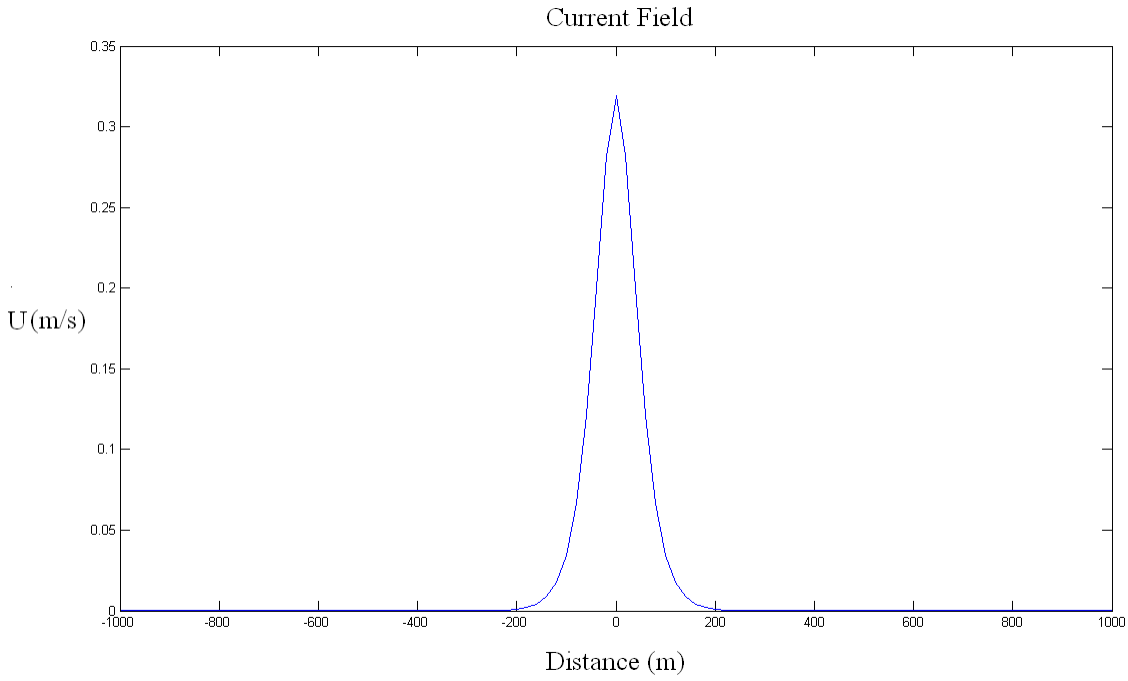

Figure 5.4 Horizontal near surface velocity in IW propagation direction with 5 m amplitude.

The model was run for different $\theta_{Look-IW}$, $\theta_{Wind-IW}$, and wind speeds. Figure 5.5 shows the definition of $\theta_{Look-IW}$ angle and $\theta_{Wind-IW}$ angle in the model. The black arrow towards east stands for IW propagation direction. The red arrow denotes the wind direction. Green arrows stand for two opposite radar look directions. $\theta_{Wind-IW}$ for simulations are 0°, $30^\circ, 60^\circ, 90^\circ, 120^\circ, 150^\circ$ and 180°. For every $\theta_{Wind-IW}$ direction, six $\theta_{Look-IW}$ angles are simulated: $0^\circ, 30^\circ, 60^\circ, 90^\circ, 120^\circ$ and 150°. For opposite look directions we get fairly similar simulation results, such as 0° and 180°, 30° and 210°, therefore only look directions with a positive down-wind component are considered in the following. All S_m values have been calculated and plotted for each condition. Figure 5.6 shows a

summary of results for an IW amplitude of 5 m. S_m is found to be larger than 1 under moderate wind speeds when $\theta_{Wind-IW}$ is less than 90°.

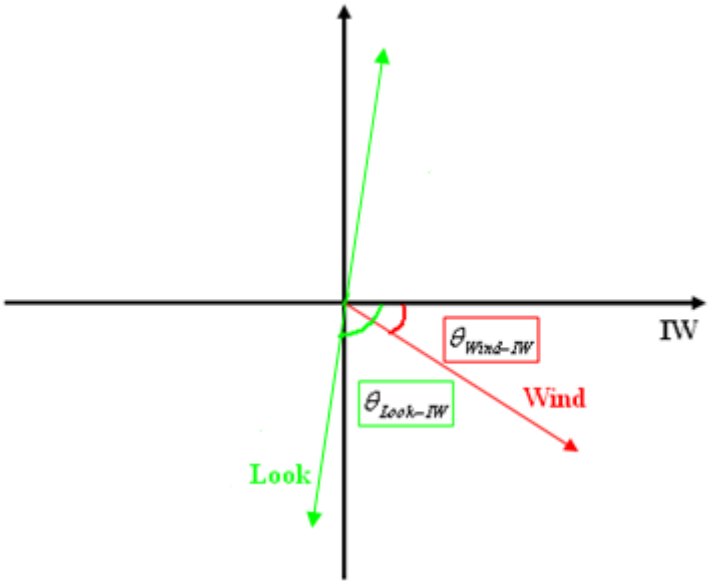

Figure 5.5 Definition of $\theta_{Look-IW}$ and $\theta_{Wind-IW}$ used in the radar imaging model.

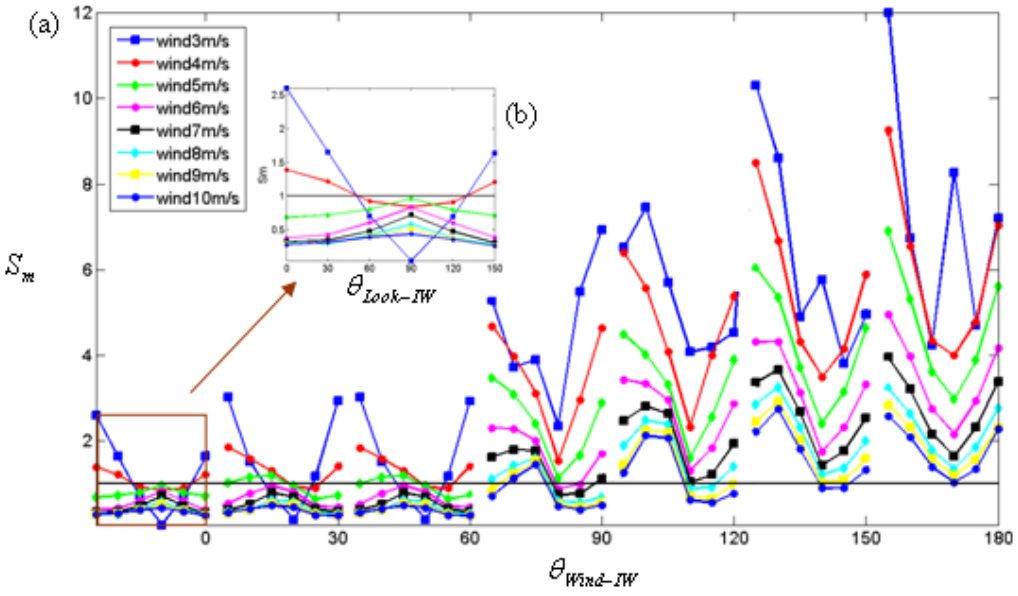

Figure 5.6 (a) S_m calculated from model simulations for different $\theta_{Look-IW}$ and $\theta_{Wind-IW}$ at different wind speeds. (b) S_m values for different $\theta_{Look-IW}$ angles when $\theta_{Wind-IW}$ is $0°$.

In the MAB, maximal IW amplitudes are over 10m in a water depth of 80 m in the SAR imaging area (Apel et al., 1997; Zheng et al., 1993) and minimal amplitudes are about 2 m. Two extra groups of simulations were run assuming IW amplitudes of 2 m and 9 m to account for this range of amplitudes (Figures 5.7 and 5.8).

Figures 5.6-5.8 illustrate that S_m values tend to increase with $\theta_{Wind-IW}$. Moreover, the proportion of S_m values larger than 1 increases with the IW amplitude when $\theta_{Wind-IW}$ is less than 90°. We can see that most model-derived S_m values are larger than 1 when the IW amplitude is 9 m (Figure 5.7) while most S_m values are less than 1 when IW amplitude is 2 m (Figure 5.8). This is not consistent with statistics results for the MAB than da Silva et al., (2002)'s result. The large observed S_m values in the MAB may be due to large IW amplitudes in the MAB. Different look directions also affect S_m at similar wind directions. However, this factor is less important since $\theta_{Look-IW}$ is predetermined by IW propagation direction. S_m values are maximal when $\theta_{Look-IW}$ is 90° and decrease towards 0° and 180°. S_m values decrease with increasing wind speed when other conditions are similar. In the MAB, observed S_m value when $\theta_{Wind-IW} > 90^\circ$ does not have a trend to be larger than the value when $\theta_{Wind-IW} < 90^\circ$ in the statistical result is mainly due to most of the S_m values are observed under the high wind conditions. It can be found that the model-derived S_m value under the high wind condition is in the range of 2-5.

It is highly possible that the relation between S_m and $\theta_{Wind-IW}$ can be different in different regions because of different typical IW amplitudes and look direction. Additionally, da Silva et al., (2002)'s finding that IWs propagating against the wind direction are imaged mostly as positive sign signatures is not always valid. It is reasonable to say that large S_m values for $\theta_{Wind-IW} < 90^{\circ}$ are highly related to large IW amplitudes, which may imply that if the IW amplitude is large then S_m value is high when $\theta_{Wind-IW}$ is small.

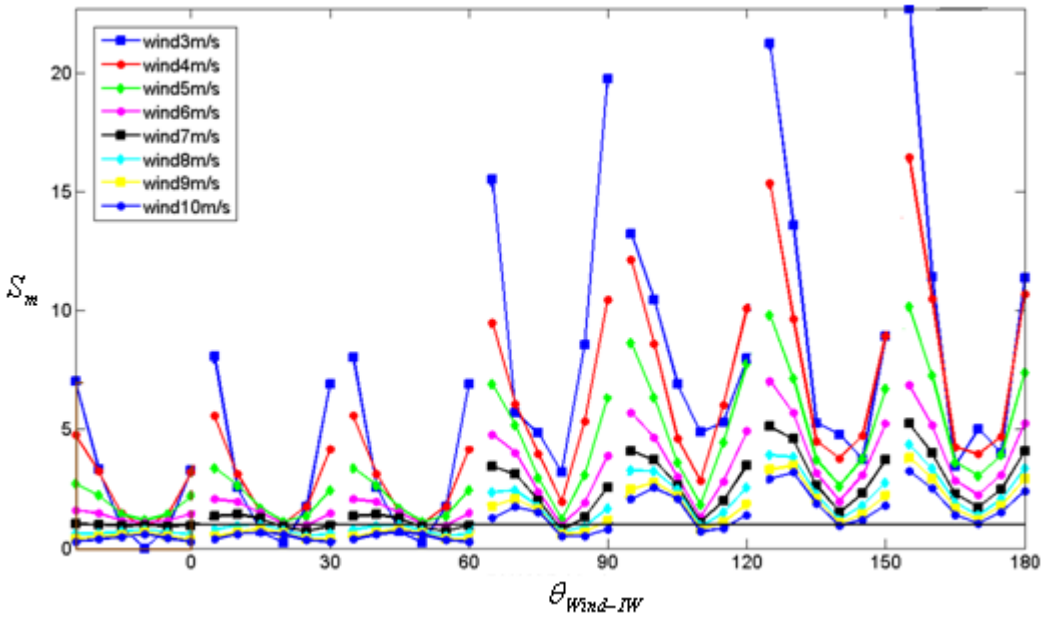

Figure 5.7 Same as Figure 5.6 for IW amplitude is 9 m

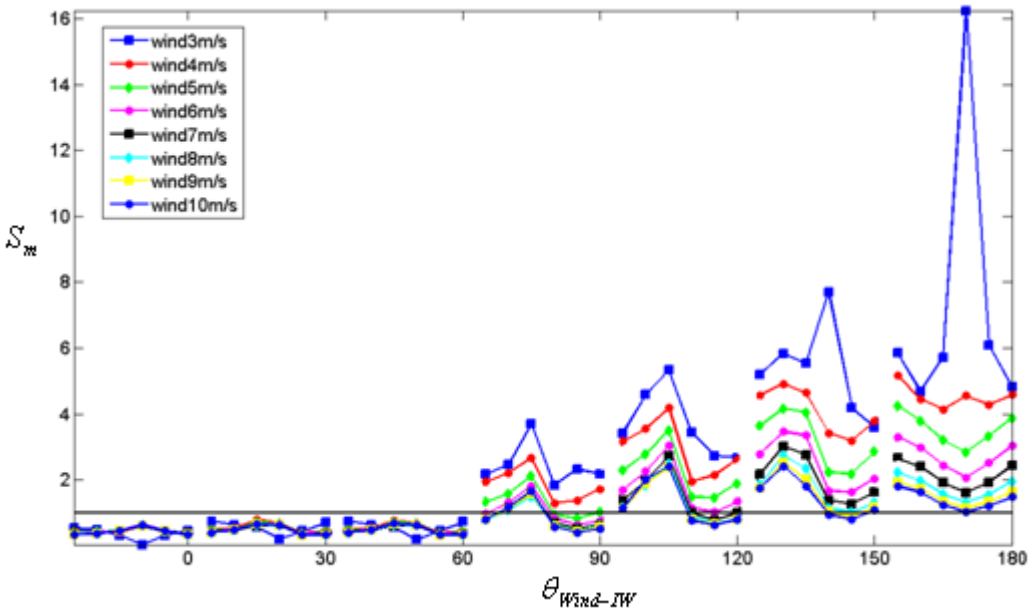

Figure 5.8 Same as Figure 5.6 for IW amplitude is 2 m

5.2 Two-soliton Interactions

Peterson and van Groesen (2000) addressed the "inverse" problem of reconstructing the amplitudes of two dimensional surface solitons from observations of wave patterns. The explicit solution to the inverse problem is derived for two interacting solitons of the KP (Kadomtsev-Petviashvili) equations. Peterson and van Groesen (2000) modeled two-soliton interactions and completed direct problem by transferring the results obtained for the two-soliton solution in phase variables to real spatial–temporal variables.

Figures 5.9 and 5.10 illustrate the relation between phase and real space variables and the dynamics of the real pattern of the two-soliton solution. When the phase shift is negative, the soliton with the larger amplitude shifts more, and the amplitude in the interaction zone increases. In contrast, when the phase shift is positive, the soliton with the larger amplitude shifts less and the amplitude in the interaction zone decreases.

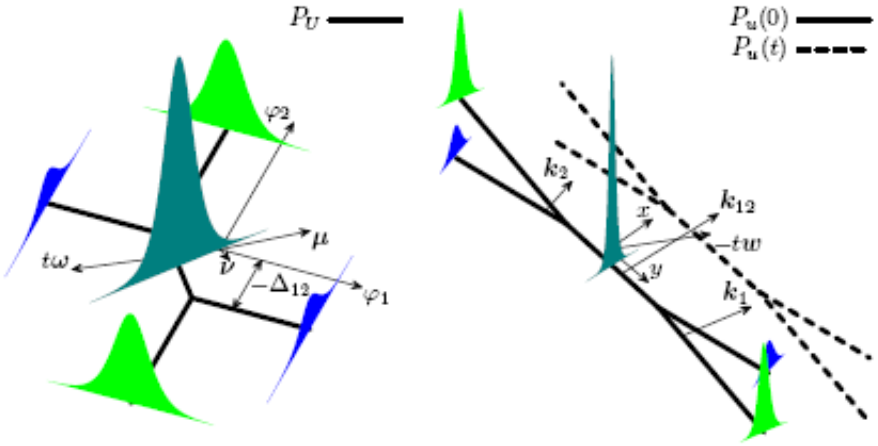

Figure 5.9 The negative phase shift case: Geometric representation of the two-soliton solution in phase variables (left) and dynamics of the two-soliton pattern in the real space-time domain (right) (Peterson and van Groesen, 2000).

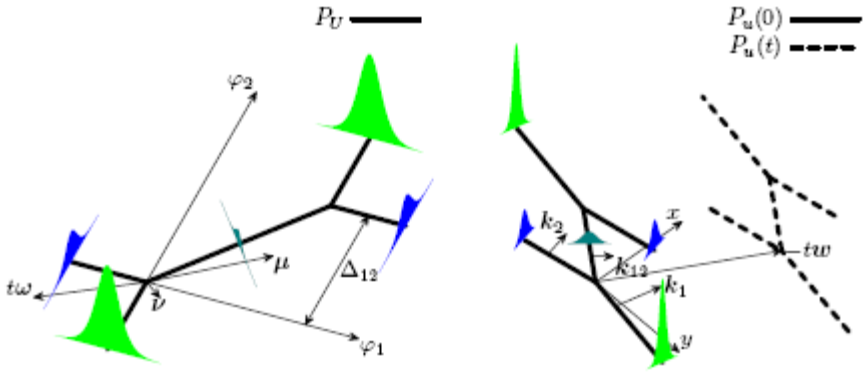

Figure 5.10 Same as Figure 5.9 for the positive phase shift case (Peterson and van Groesen, 2000)

Figure 5.11 shows a sketch of the leading wave crests in the interaction pattern in Figure 4.8. It agrees reasonably with the negative phase shift case shown in Figure 5.9. IW1 with a larger amplitude has a smaller shift, and IW2 with a smaller amplitude has a larger shift.

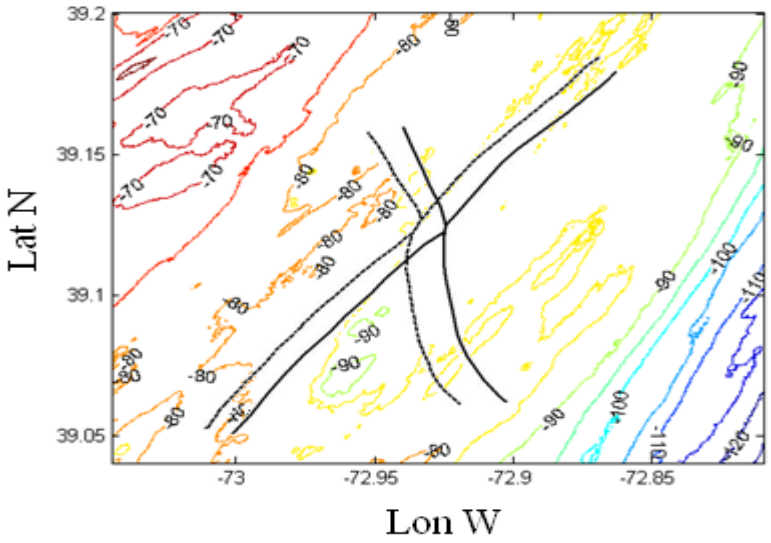

Figure 5.11 Sketch of the two leading wave crests in the interaction pattern of Figure 4.9.

The intensity profile of the interaction zone is plotted in Figure 5.12. Its positive modulation is 0.63, larger than that of the four parts (Figure 4.10). We can infer that the amplitude of the interaction center is larger than that of the two IWs after interaction, which fits the negative phase case.

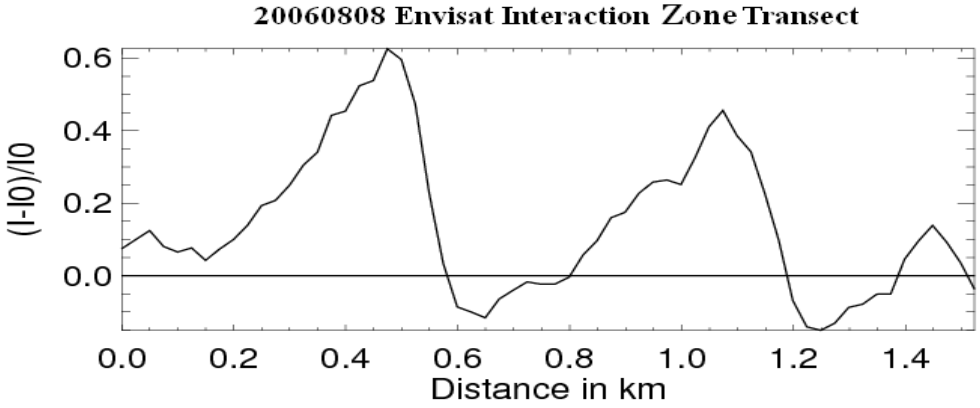

Figure 5.12 Relative intensity transect in the interaction zone of the pattern in Figure 4.8.

CHAPTER 6 SUMMARY AND CONCLUSIONS

In order to better understand the occurrence of IW signatures and their dependence of IW signature types on wind condition, 57 SAR images of the MAB, acquired between July and September 2006, have been analyzed. BlendQScat data and ASIS buoy measurements were used to estimate wind speeds and directions. A statistical analysis of the relationship between S_m values and $\theta_{Wind-IW}$ was carried out and a radar imaging model was used to explain deviations from the results of da Silva et al. (2002). Another focus of the study has been on IW interaction. A unique combination of available SAR images and in-situ measurements has made this study possible. The primary results can be summarized as followed:

1) The occurrence of IW signatures in the MAB is highly dependent on the wind speed. Moderate wind speeds of 4-7 m/s are favorable for imaging IW signatures by SAR, whereas very few IW signatures are observed when the wind speed is higher than 10 m/s and lower than 2 m/s. Approximately 61% of IW signature occurrences fall into the moderate wind speed range. These results are consistent with those found in other areas, such as the South China Sea.
2) Over 150 relative intensity profiles in the observed IW fields have been analyzed, and S_m values of the leading IW in every packet have been calculated. Statistical results of the relationship between S_m values and $\theta_{Wind-IW}$ in the MAB show that there are many S_m values larger than 1 even when $\theta_{Wind-IW}$ is less than 90°, which does not agree with the results of da Silva et al. (2002), who found

illustrated that most statistic results S_m values were less than 1 when $\theta_{Wind-IW}$ was less than 90° in the western Iberian shelf.

3) A state of the art radar imaging model has been used to explain the statistical results for the MAB. The model was run for different $\theta_{Wind-IW}$ and $\theta_{Look-IW}$ and three different IW amplitudes. In the case of 2 m IW amplitude, most S_m values are less than 1, similar to the findings of da Silva et al. (2002). In the case of 5 m IW amplitude, many model-derived S_m values in the moderate wind speed range are larger than 1. In the case of an IW amplitude of 9 m, most model-derived S_m values are larger than 1 even at very small $\theta_{Wind-IW}$. Overall, the model results indicate that the proportion of S_m values larger than 1, when $\theta_{Wind-IW}$ is less than 90°, increases with the IW amplitude. In the MAB, the IW amplitude has a range of 2-10 m. The large proportion of S_m values in this area may be due to high IW amplitudes. In general, relating IW signature types mainly to the wind direction is an oversimplification without considering other factors such as radar look direction and IW amplitude.

4) An IW interaction pattern has been studied on the basis of two sequential SAR images with a time lag of 28 minutes and temperature and current measurements from three moorings. First, phase velocities of four parts of the X-shaped IW signature pattern were estimated by correlation methods using two sequential images. The phase velocities can also be estimate from SAR images and moorings current records, which agree well with the result estimated by the correlation method. IW2 has a large phase velocity change from 0.94 m/s to 0.65 m/s due to

the interaction while the IW1 velocity does not change much. The large velocity change in IW2 explains the distortion in the interaction part after 28 minutes in the ERS2 image. Second, the relative intensity changes before and after the interaction along wave crest which indicates an energy exchange due to the interaction. In addition, a particularly strong IW intensity in the interaction zone indicates an amplitude increase due to the interaction. Third, although we cannot get an accurate estimate, we can be sure that IW1 has a larger amplitude than IW2 from the temperature records. IW1, with a larger amplitude, shifts less while IW2, with a smaller amplitude, shifts more due to the interaction. Altogether all the behaviors are consistent with the dynamics of two-soliton pattern with a negative phase shift derived from KP equation according to Peterson and van Groesen (2000).

REFERENCES

Alpers, W., 1985. Theory of radar imaging of IWs. Nature, 314, 245-247.

Anctil, F., M.A. Donelan, W. M. Drennan, and H. C. Graber, 1994. Eddy correlations measurements of air-sea fluxes from a discus buoy. J. Atmos. Oceanic Technol., 11, 1144-1150.

Apel, J. R., et al., 1997. An overview of the 1995 SWARM shallow water IW acoustic scattering experiment, IEEE J. Oceanic Eng., 22, 465–500.

Apel, J. R., Jackson, C. R., 2004. Synthetic Aperture Radar Marine Users Manual Washington, DC: NOAA (2004) M.

Araujo, I.B., Da Silva, J.C.B., Ermakov, S.A. and Robinson, I.S., 2002. On the role of wind direction in ERS SAR signatures of IWs on the Iberian shelf. Global Atmosphere and Ocean System, 8, (4), 269-281.

Brandt, P., Romeiser, R., and Rubino, A., 1999. On the determination of characteristics of the interior ocean dynamics from radar signatures of internal solitary waves. Journal of Geophysical Research C: Oceans 104 (C12), pp. 30039-30045.

Bogucki, D., T. Dickey, and L. G. Redekopp, 1997. Sediment resuspension and mixing by resonantly generated internal solitary waves. J. Phys. Oceanogr., 27, 1181–1196.

Caruso, C.M., Graber, H.C., 2006. NLIWI Mid-Atlantic Bight Satellite Data Summary (unpublished).

Chen, C.Y., 2007. An experimental study of stratified mixing caused by internal solitary waves in a two-layered fluid system over variable seabed topography. Ocean Engineering 34 (14–15), 1995–2008.

Chen, C.Y., Hsu, J.R.C., 2005. Interaction between IWs and a permeable seabed. Ocean Engineering 32 (5–6), 587–621.

Chen, C.Y., Hsu, J.R., Chen, H.H., Kuo, C.F., Cheng, M.H., 2007. Laboratory observations on internal solitary wave evolution on steep and inverse uniform slopes. Ocean Engineering 34 (1), 157–170.

Chin, T.M., R.F. Milliff, and W.G. Large, 1998. Basin-scale, high-wavenumber sea surface wind fields from a multiresolution analysis of scatterometer data. Journal of Atmospheric and Oceanic Technology, 15, 741-763.

Da Silva, J. C. B., Ermakov, S.A., Robinson, I.S., Jeans, D.R.G., and Kijashko, S.V., 1998. Role of surface films in ERS SAR signatures of IWs on the shelf, 1: Short-period IWs. Journal of Geophysical Research, 103, 8009–8031.

Da Silva, J.C.B., Ermakov, S.A., Robinson, I.S., Potter, R.C.H., 1999. ERS-SAR observation of long IWs with positive backscatter signature. International Geoscience and Remote Sensing Symposium (IGARSS) 3, pp. 1481-1483.

Drennan, W.M. and L. K. Shay, 2006. On the variability of the fluxes of momentum and sensible heat, Boundary-Layer Meteorology, 119, 81-107.

Holligan, P. M., RD Pingree and GT Mardell, 1985. Oceanic solitons, nutrient pulses and phytoplankton growth. Nature, 314: 348-350.

Holloway, P.E., Pelinovsky, E., Talipova, T., & Barnes, B., 1997. A nonlinear model of internal tide transformation on the Australian North West Shelf. Journal of Physical Oceanography, 27, 871– 893.

Hsu, M. K., Liu, A.K., and Liu, C., 2000. A study of IWs in the China Seas and Yellow Sea using SAR. Continental Shelf Research, 20, 389–410.

Huang, W., Gan, X., Yang, J., Fu, B., Chen, P. 2009. Role of surface winds in SAR signatures of oceanic IWs in the northern South China Sea. Proceedings of SPIE, the international society for optical engineering 7473, art. no. 74730K.

Irish, J.D., Lynch, J.F., Kemp, J.N., Duda, T.F., Newhall, A.E., 2004. A moored array for measuring internal solitary waves during shallow water 06. Oceans Conference Record (IEEE), art. no. 4449170.

Killworth, P., 1998. Something stirs in the deep. Nature, 396(24/31), 720 – 721.

Laur, H., 1992. Derivation of backscattering coefficient in ERS-1.SAR.PRI products, in ERS-1. SAR Calibration, ESA Rep.1, European Space Agency, Paris.

Li, X., Clemente-Colon, P., and Friedman, K., 2000. Estimating oceanic mixed layer depth from IW evolution observed from RADARSAT-1 SAR. Johns Hopkins University Applied Physics Lab Technical Digest, 21(1), 130-135.

Li, H., He, Y., Du, T., Shen, H., 2006. Effects of winds on Internal wave synthetic aperture radar images. Geoscience and Remote Sensing Symposium.

Liu, A.K., 1988. Analysis of nonlinear IWs in the New York Bight. Journal of Geophysical Research, 93, 12317–12329.

Liu, A.K., Chang, Y.S, Hsu, M.K., Liang, N.K., 1998. Evolution of nonlinear IW in the East and South China Sea. Journal of Geophysical Research, 103 (C4): 7995-8008.

Liu, A.K., Ramp, S.R., Zhao, Y., Tang, T.Y., 2004. A case study of internal solitary wave propagation during ASIAEX-2001. IEEE J. Oceanic Engineering, 29, 1144-1156.

Mitnik, L.M., Dubina, V.A., 2007. Spatial-temporal distribution and characteristics of IWs in the Okhotsk and Japan seas studied by ERS-1/2 SAR and ENVISAT ASAR, 2007. European Space Agency, (Special Publication) SP (SP-636).

Newhall, A.E., Duda, T.F., Von der Heydt, K., Irish, J.D., Kempt, J.N., Lerner, S.A., Liberatore, S.P., Lin, Y.T., Lynch, J.F., Maffei, A.R., Morozov, A.K., Shmelev, A., Sellers, C.J., Witzell, W.E., 2007. Acoustic and oceanographic observations and configuration information for the WHOI moorings from the SW06 experiment. Woods Hole Oceanographic Institution Technical Report WHOI-2007-04, pp. 117.

Peterson, P., and van Groesen, E., 2000. A direct and inverse problem for wave crests modelled by interactions of two solitons. Physica D, 141:316--332.

Phillips, O. M., 1977. The Dynamics of the Upper Ocean, 2nd Ed., Cambridge University Press, New York.

Porter, D.L., and D.R. Thomson, 1999. Continental shelf parameters inferred from SAR IW observations, Journal of Atmospheric and Oceanic Technology, 16, 475-487.

Romeiser, R., Schmidt, A. and Alpers, W., 1994. A three-scale composite surface model for the ocean wave-radar modulation transfer function. Journal of Geophysical Research, 99, 9785-9801.

Romeiser, R., W. Alpers, and V. Wismann, 1997. An improved composite surface model for the radar backscattering cross section of the ocean surface, 1. Theory of the model and optimization / validation by scatterometer data, Journal of Geophysical Research, *102*, 25,237-25,250.

Romeiser, R. and Alpers, W., 1997. An improved composite surface model for the radar backscattering cross section of the ocean surface, 2, Model response to surface roughness variations and the radar imaging of underwater bottom topography. Journal of Geophysical Research, 102, 25,251-25,267.

Yang, J. S., Huang, W. G., Zhou, C. B., and Xiao, Q. M., 2001. Simulation Study on Optimal Conditions for Internal Wave Observation by SAR, IGARSS'2001.

Yang, J., Huang, W., Zhou, C., Hsu, M.K., Xiao, Q., 2003. Nonlinear IW amplitude remote sensing from SAR imagery. Proceeding of SPIE, 4892, 450.

Zheng, Q., Yan, X.H., and Klemas, V., 1993. Statistical and Dynamical Analysis of Internal Waves on the Continental Shelf of the Middle Atlantic Bight from Space Shuttle Photographs. Journal of Geophysical Research, 98, 8495–8504.

Zhao, Z., Klemas, V., Zheng, Q., Li, X., Yan, X.H., 2004. Estimating parameters of a two-layer stratified ocean from polarity conversion of internal solitary waves observed in satellite SAR images. Remote Sensing of Environment, 92, 276-287.

Zhao, Y., Liu, A.K. and Hsu, M.K., 2008. Internal wave refraction observed from sequential satellite images. International Journal of Remote Sensing, 29, 6381-6390.

Zheng, Q., Yuan, Y., Klemas, V. and Yan, X.H., 2001. Theoretical expression for an ocean internal soliton synthetic aperture radar image and determination of the soliton characteristic half width. Journal of Geophysical Research, 106, 31415-31423.

Zheng, Q., Susanto, R.D., Ho, C.R., Song, Y.T., and Xu, Q., 2007. Statistical and dynamical analyses of generation mechanisms of solitary IWs in the northern South China Sea. Journal of Geophysical Research, 112(C3), C03021.